



1 Colorado air quality impacted by long range transport: A set of 2 case studies during the 2015 Pacific Northwest fires

3 Jessie M. Creamean^{1,2*}, Paul. J. Neiman², Timothy Coleman^{1,2}, Christoph J. Senff^{1,3}, Guillaume
4 Kirgis^{1,3}, Raul J. Alvarez³, and Atsushi Yamamoto⁴

5 ¹University of Colorado at Boulder, Cooperative Institute for Research in Environmental Sciences, Boulder, CO,
6 80309, USA

7 ²NOAA Earth System Research Laboratory, Physical Sciences Division, Boulder, CO, 80305, USA

8 ³NOAA Earth System Research Laboratory, Chemical Sciences Division, Boulder, CO, 80305, USA

9 ⁴Process and Environmental, HORIBA, Instruments, Inc., Irvine, CA, 92618, USA

10 *Correspondence to:* Jessie M. Creamean (jessie.creamean@noaa.gov)

11 **Abstract.** Biomass burning plumes containing aerosols from forest fires can be transported long distances, which can
12 ultimately impact climate and air quality in regions far from the source. Interestingly, these fires can inject aerosols
13 other than smoke into the atmosphere, which very few studies have evidenced. Here, we demonstrate a set of case
14 studies of long-range transport of mineral dust aerosols in addition to smoke from numerous forest fires in the Pacific
15 Northwest to Colorado, U.S. These aerosols were detected in Boulder, Colorado along the Front Range using Beta-
16 ray attenuation and energy dispersive X-ray fluorescence spectroscopy, and corroborated with satellite-borne lidar
17 observations of smoke and dust. Further, we examined the transport pathways of these aerosols using air mass
18 trajectory analysis and regional and synoptic scale meteorological dynamics. Three separate events with poor air
19 quality and increased mass concentrations of metals from biomass burning (S and K) and minerals (Al, Si, Ca, Fe, and
20 Ti) occurred due to the introduction of smoke and dust from regional and synoptic scale winds. Cleaner time periods
21 with good air quality and lesser concentrations of biomass burning and mineral metals between the haze events were
22 due to the advection of smoke and dust away from the region. Dust and smoke present in biomass burning haze can
23 have diverse impacts on visibility, health, cloud formation, and surface radiation. Thus, it is important to understand
24 how aerosol populations can be influenced by long-range transported aerosols, particularly those emitted from large
25 source contributors such as forest fires.

26 **Keywords.** Aerosol transport, air quality, mineral dust, biomass burning, remote sensing, in situ observations

27 1 Introduction

28 Wildfires in both forested and agricultural regions serve as a steady source of pollutants into the atmosphere. Gas
29 phase constituents such as methane (CH₄), carbon monoxide (CO), carbon dioxide (CO₂), sulphur dioxide (SO₂) and
30 nitrogen oxides (NO_x; NO + NO₂) can be produced from burning of biofuels (Gadi et al., 2003; Radojevic, 2003), in
31 addition to precursors that induce ozone production (Jaffe and Wigder, 2012). Additionally, wildfires produce large
32 concentrations of aerosols which are injected into the atmosphere or formed in the smoke plume via secondary
33 processes and include carbonaceous species (elemental and organic carbon) (Park et al., 2003; Spracklen et al., 2007)



34 and biogenic heavy metals (including but not limited to Fe, Mn, Cd, Cu, Pb, Cr, and Ni) (Nriagu, 1989; Radojevic,
35 2003). Soluble inorganic species such as sulphate, nitrate, ammonium, and chloride are found in fire emissions and
36 partitioned to the particle phase through heterogeneous reactions with the gas phase species released during the
37 combustion process (Pio et al., 2008). Strong, turbulent winds inside combustion zones from controlled and wild
38 vegetation fires can introduce considerable amounts of dust particles into the free troposphere, which can subsequently
39 be transported over thousands of kilometres with the smoke (Clements et al., 2008; Ansmann et al., 2009; Baars et al.,
40 2011). However, few studies have documented how wildfires inject mineral dust into the atmosphere (Gaudichet et
41 al., 1995; Chalbot et al., 2013; Yang et al., 2013; Nisantzi et al., 2014), particularly in heavily forested or agricultural
42 regions such as the Pacific Northwest of the U.S. where dust sources are limited relative to arid regions in Africa, the
43 Middle East, and Asia. Prescribed burning (i.e., slash-and-burn techniques) and wildfires are common in these arid
44 “dust belt” regions, inducing the simultaneous emission of dust and smoke (Streets et al., 2003; Pinker et al., 2010).

45

46 Aerosols produced directly from wildfires (i.e., carbonaceous and soluble inorganic particulates) or injected into the
47 free troposphere from smoke plume dynamics (i.e., mineral dust) have diverse effects on climate and air quality. For
48 instance, hygroscopic organic aerosol, sulphate, and nitrate can enable aerosols to serve as cloud condensation nuclei
49 (CCN) (Cruz and Pandis, 1997), whereas mineral dust and black carbon are effective ice nucleating particles (INPs)
50 at sub-freezing temperatures (DeMott et al., 1999; DeMott et al., 2003; Vali et al., 2015). Both of these aerosol nuclei
51 modify cloud radiative properties, lifetime, and impact precipitation formation, and have been shown to originate from
52 prescribed burns and wildfires (Eagan et al., 1974; McCluskey et al., 2014). Enhanced pollutants from fires also
53 severely influence air quality, and can prompt adverse health effects (Bravo et al., 2002; Phuleria et al., 2005;
54 Wiedinmyer et al., 2006). For instance, smoke plumes from wildfires have been linked to childhood mortality
55 (Jayachandran, 2008), asthma (Bowman and Johnston, 2005), and various respiratory illness and diseases (Mott et al.,
56 2002; Moore et al., 2006). These effects are additionally complicated by aging from biogenic gases in the smoke
57 plume during transport. Further, previous air quality studies on the East Coast of the U.S. have shown that enhanced
58 aerosol optical depths associated with both wildfires and anthropogenic sources can cause large errors in
59 meteorological models used to forecast poor air quality events (Zamora et al., 2005). Overall, the aerosol species
60 emitted or formed from wildfire plumes are complex in nature and possess several diverse climate and health effects,
61 thus demonstrating the need to better understand the various types, sources, and transport pathways of these emissions.

62

63 Air quality is strongly dependent not only on emission sources such as wildfires, but also on weather and climate
64 change (Jacob and Winner, 2009). Regions with complex topography such as the Front Range of Colorado, U.S. (see
65 Figure 1) have unique meteorological phenomena such as upslope/downslope flows that serve as agents for focusing
66 or cleaning out local air pollution from the Denver metropolitan area (Haagenson, 1979). Typically, this region is
67 characterized by good air quality in terms of particulate matter (PM) relative to other larger urban and industrial areas,
68 although it experiences occasional pollution episodes due to modulation of the mountain slope dynamics, oil and
69 natural gas production, and wildfires (Watson et al., 1998; Sibold and Veblen, 2006; Brown et al., 2013). Here, we
70 show that the Front Range air quality was severely impacted by long-range transported wildfire emissions from the



71 Pacific Northwest during Aug 2015. A reoccurring influx of pollutants, including SO₂, NO_x, and smoke aerosols,
72 infiltrated the Front Range region due to shifts in regional and synoptic scale meteorology. Interestingly, mineral dust
73 was also transported with the smoke plume to the Front Range from the wildfires. This complex mixture of gases and
74 aerosols can have numerous climate and health effects in the region, and should be evaluated to develop a better
75 understanding of future influences from wildfire emissions, especially considering a warmer and drier climate will
76 potentially lead to more frequent wildfires (Westerling et al., 2006; Liu et al., 2010).

77 2 Methods

78 2.1 Satellite observations

79 The source of aerosols from the fires was determined using imagery from the Moderate Resolution Imaging
80 Spectroradiometer (MODIS) on board the Terra satellite. MODIS is a multi-spectral sensor with 36 spectral bands,
81 ranging in wavelength from 0.4 to 14.2 μm. Aerosol optical depth (AOD) data from MODIS were acquired from the
82 Giovanni data server (<http://giovanni.gsfc.nasa.gov/giovanni/>) for daily AOD at a 1° spatial resolution using a domain
83 of 82°W to 163°W and 26°N to 59°N (MOD08_D3_051). MODIS AOD is retrieved from three spectral channels
84 (0.47 μm, 0.66 μm, and 2.1 μm) using the algorithm described by Kaufman et al. (1997) in cloud-free pixels (10 km
85 x 10 km grid box) (Ackerman et al., 1998). Fire and surface thermal anomaly data were also acquired from the MODIS
86 Terra satellite using brightness temperature measurements in the 4-μm and 11-μm channels
87 (<https://earthdata.nasa.gov/labs/worldview/>) (Giglio, 2010). The fire detection strategy is based on absolute detection
88 of a fire (when the fire strength is sufficient to detect), and on detection relative to its background (to account for
89 variability of the surface temperature and reflection by sunlight) (Giglio et al., 2003). The algorithms include masking
90 of clouds, bright surfaces, glint, and other potential false alarms (Giglio et al., 2003). Swaths from overpasses over
91 the Pacific Northwest were used to determine the locations of fires on a daily basis.

92
93 In order to evaluate the types of aerosols present in enhanced AOD plumes over the western U.S., aerosol subtype
94 data were retrieved from Cloud-Aerosol Lidar with Orthogonal Polarization (CALIOP) on board Cloud-Aerosol Lidar
95 and Infrared Pathfinder Satellite Observations (CALIPSO). Level-2 ValStage1 V.30 Vertical Feature Mask data
96 obtained from NASA's Earth Observing System Data and Information System (EOSDIS;
97 <https://search.earthdata.nasa.gov/>) contain vertically-resolved data of aerosol layer sub-type, including but not limited
98 to smoke, dust, and polluted dust (i.e., dust mixed with smoke) (Vaughan et al., 2004; Omar et al., 2009; Winker et
99 al., 2009). CALIPSO was launched on 28 Apr 2006 and flies in an orbital altitude of 705 km as part of the sun-
100 synchronous "A-train" satellite constellation. CALIOP is an elastic backscatter lidar operating at 532 nm and 1064
101 nm, completed with a depolarization channel at 532 nm to enable detection of aerosols and clouds. Granule data were
102 acquired from orbital swaths that passed over the north-western U.S. (domain includes Washington, Oregon, northern
103 California, Idaho, Nevada, Montana, Wyoming, Utah, and Colorado) from 15 Aug to 2 Sep 2015 and processed using
104 modified Python code developed by the Hierarchical Data Format (HDF) group at the University of Illinois, Urbana-
105 Champaign (<http://hdfeos.org/>). Aerosol sub-types were also examined off the U.S. West Coast across the central



106 North Pacific Ocean, in the context of air mass trajectory analysis, to ensure mineral dust and smoke were transported
107 to Colorado from the Pacific Northwest fires rather than from deserts or fires overseas.

108 **2.2 Colorado air quality data**

109 All air quality data were acquired from the Colorado Department of Public Health and Environment (CDPHE;
110 <http://www.colorado.gov/airquality/report.aspx>) from 15 Aug to 2 Sep 2015 at various sites throughout the Colorado
111 Front Range (see Figure 1). Table 1 provides the site latitudes, longitudes, elevations, and which measurements were
112 available at each site. Hourly measurements included mass concentrations ($\mu\text{g m}^{-3}$) of particulate matter for particles
113 with diameters $\leq 2.5 \mu\text{m}$ ($\text{PM}_{2.5}$) and $\leq 10 \mu\text{m}$ (PM_{10}). Carbon monoxide (CO), sulphur dioxide (SO_2), nitric oxide
114 (NO), nitrous oxide (NO_2), and ozone (O_3) were also evaluated but no significant differences were observed between
115 haze and non-haze time periods, thus the data are not presented. All times shown are coordinated universal time [UTC;
116 local time or mountain daylight time (MDT) + 6].

117 **2.3 In situ aerosol observations at Boulder, Colorado**

118 Real-time, hourly ambient aerosols samples were analysed for $\text{PM}_{2.5}$ total mass concentrations ($\mu\text{g m}^{-3}$) and
119 concentrations of various metals (ng m^{-3}) using the HORIBA, Ltd. PX-375 continuous particle mass and elemental
120 speciation monitor (<http://www.horiba.com/process-environmental/products/ambient/details/continuous-particulate-monitor-with-x-ray-fluorescence-px-375-27871/>) from 26 Aug to 2 Sep 2015 at the National Oceanic and
122 Atmospheric Administration (NOAA) David Skaggs Research Centre (DSRC) located in Boulder, Colorado (39.99°N,
123 105.26°W, and 1672 m MSL; see Figure 1). The PX-375 draws in air at 16.7 L min^{-1} through a U.S. Environmental
124 Protection Agency (EPA) Louvered PM_{10} inlet, then subsequently passes through a BGI Very Sharp Cut Cyclone
125 (VSCC™) to filter for particles smaller than $2.5 \mu\text{m}$ in diameter. Air is pulled through a nozzle for 60 minutes per
126 hourly sample, where particles are subsequently deposited in a 100-mm diameter spot on Teflon™ PTFE fabric filter
127 tape for analysis. Once the sample is collected for 60 minutes, beta-ray attenuation and energy dispersive X-ray
128 fluorescence spectroscopy (EDXRF) analyses are conducted for 60 minutes and 1000 seconds, respectively, per hourly
129 sample, simultaneous to the sampling of the subsequent sample. Beta-ray attenuation analysis is used to measure total
130 $\text{PM}_{2.5}$ mass concentrations and EDXRF is used to analyse concentrations of Ti, V, Cr, Mn, Fe, Ni, Cu, Zn, As, Pb, Al,
131 Si, S, K, and Ca. The EDXRF unit contains a CMOS camera for sample images. Calibration material used for X-ray
132 intensity is NIST SRM 2783. Lower detection limits (LDLs) are shown in Table 2 and error was calculated to be $\pm 2\%$
133 for hourly metal concentrations. Hourly total $\text{PM}_{2.5}$ mass concentrations had an LDL of $2.00 \mu\text{g m}^{-3}$.

134 **2.4 Aerosol and ozone remote sensing observations at Boulder, Colorado**

135 The Tunable Optical Profiler for Aerosol and oZone (TOPAZ) lidar was operated at the DSRC on 9 days from 14 Aug
136 through 2 Sep 2015 and it collected about 62 hours of ozone and aerosol profile data, primarily between mid-morning
137 and early evening local time. TOPAZ is a state-of-the-art, tunable ozone differential absorption lidar. It emits pulsed
138 laser light at three ultraviolet wavelengths between 285 and 295 nm and measures ozone as well as aerosol backscatter
139 and extinction profiles with high temporal and spatial resolutions (Alvarez et al., 2011). The TOPAZ lidar is mounted



140 in a truck with a rooftop two-axis scanner. This scanner permits pointing the lidar beam at elevation angles between
141 -5 and 30 degrees at a fixed but changeable azimuth angle. To achieve zenith operation the scanner mirror is moved
142 out of the beam path. Typical TOPAZ operation consists of a scan sequence at 2 , 6 , 20 , and 90 degrees elevation,
143 repeated approximately every five minutes. The range-resolved ozone and aerosol observations at the shallow
144 elevations angles are projected onto the vertical and spliced together with the zenith observations, resulting in
145 composite vertical ozone and aerosol profiles from about 15 m to $2-3$ km above ground level (AGL) at five minutes
146 time resolution (Alvarez et al., 2012). In this study, we only used the lidar aerosol extinction profiles measured at a
147 wavelength of 294 nm. The aerosol profile retrieval requires assumptions about the lidar calibration constant and the
148 aerosol extinction-to-backscatter or lidar ratio. For this study we used an altitude-constant lidar ratio of 40 sr, which
149 is a good approximation for continental and urban aerosols. The lidar signal at the aerosol wavelength of 294 nm is
150 also affected by ozone absorption. Therefore, uncertainties in the ozone observations can cause biases in the aerosol
151 retrieval. This, combined with uncertainties in the calibration constant and lidar ratio, can lead to errors in the aerosol
152 extinction coefficient profiles of up to about 30% . The precision of the 5-minute aerosol extinction measurements is
153 typically better than 10% .

154 **2.5 Meteorological data and analysis**

155 A gridded perspective of synoptic-scale conditions across North America was provided using the NOAA/National
156 Centres for Environmental Prediction (NCEP) Rapid Refresh numerical data package [RAP;
157 <http://rapidrefresh.noaa.gov/> (Benjamin et al., 2016)]. The RAP is an operational assimilation/modelling system
158 updated hourly, with 13 -km horizontal resolution and 50 vertical levels.

159

160 Air mass backward trajectory analyses were conducted using HYSPLIT 4 (Draxler and Rolph, 2011) and data from
161 the NOAA/NCEP Global Data Assimilation System (GDAS) (Kalnay et al., 1996). HYSPLIT trajectories do not
162 include processes that may affect particle concentrations such as convective transport, wet removal, or dry removal,
163 and are only intended to highlight the possible transport pathways. To study the potential for transport from the Pacific
164 Northwest fires region, and to eliminate potential contribution from aerosol sources overseas, we used an ensemble of
165 backward trajectories initiated at multiple altitudes and times ending above the NOAA building in Boulder. Ten-day
166 back trajectories were initiated every 6 hours (at $00:00$, $06:00$, $12:00$, and $18:00$ UTC) during 15 Aug–2 Sep 2015 at
167 500 , 1000 , and 2000 m AGL (corresponds to 2172 , 2672 , and 3672 m MSL).

168

169 A 449 -MHz wind profiler (White et al., 2013), deployed near the Boulder Atmospheric Observatory in Erie, Colorado
170 (BAO; 40.05°N , 105.01°W , and 1577 m MSL; location shown in Figure 1), provided hourly-averaged profiles of
171 horizontal wind. The high (low) mode extended from 145 m (195 m) to 10074 m (5059 m) AGL with a vertical
172 resolution of 200 m (100 m). The wind-profiler data were edited objectively using the vertical-temporal continuity
173 method of Weber et al. (1993) and then subjected to additional manual editing as needed. For the purpose of this study,
174 we utilized only the low-mode observations.



175 3 Results and discussion

176 3.1 Haze events induced poor air quality along Colorado's Front Range

177 The shift in air quality was evident during three August haze events in the Denver metro area. Figure 2 shows photos
178 of notable air quality transitions in Denver looking westward towards the foothills of the Rocky Mountains. The image
179 on 15 Aug shows typical, clean conditions, where the foothills were visible west of Denver. On 17 Aug, a haze settled
180 in the region, creating a low-level pollution plume that masked the view of the foothills. This haze continued to
181 infiltrate the Denver metro area, reaching the poorest visibility on 23 Aug. This haze persisted in the Denver metro
182 area until 27 Aug, when clear conditions were re-established and the foothills were once again visible. However, the
183 air quality deteriorated once again by 29 Aug, with hazy conditions obscuring the foothills. This haze event was shorter
184 lived, clearing out once again on 31 Aug. The cleaner conditions persisted until the end of the measurement period on
185 2 Sep. The qualitative observations of the three separate haze events were corroborated by in situ air quality
186 measurements along the Front Range. Figure 3 shows hourly and daily averaged $PM_{2.5}$ mass concentrations (herein,
187 simply called " $PM_{2.5}$ ") at the sites provided in Table 1. Overall, three separate haze events occurred along the Front
188 Range with the worst days visually observed (Figure 2) on the 17, 23, and 29 Aug (events 1, 2, and 3, respectively),
189 when $PM_{2.5}$ reached maximum concentrations and a cold front passed through (discussed in section 3.3). Prior to each
190 of these events, $PM_{2.5}$ was suppressed then slowly increased to each event's maximum concentrations on 17, 23, and
191 29 Aug. $PM_{2.5}$ slowly decreased following each of these haze events. PM_{10} (not shown) did not follow similar
192 increases and decreases as the $PM_{2.5}$, suggesting the smaller particles contributing to $PM_{2.5}$ originated from different,
193 likely more distant sources as compared to coarser particles contributing to the PM_{10} , which are likely from more
194 local sources (VanCuren, 2003; Neff et al., 2008).

195 3.2 Biomass burning plume propagates towards Colorado

196 During the 15 Aug–2 Sep time period, fires in both forested and agricultural vegetation areas and to some extent in
197 shrub and grasslands in the Pacific Northwest were prominent. Figures 4–6 show MODIS retrievals of fire hotspots
198 and aerosol optical depth (AOD) during the first, second, and third haze events in Colorado, when numerous fires
199 were detected in Washington, Oregon, northern California, northern Idaho, and north-western Montana. Three cases
200 are defined as the time periods surrounding and including the haze event days: Case 1 (15–18 Aug), Case 2 (20–23
201 Aug), and Case 3 (26–29 Aug).

202

203 On 15 Aug, prior to the onset of the first haze event in Colorado, the plume of enhanced AOD propagating from the
204 fires in the Pacific Northwest remained north of Colorado in Montana and southern Canada (Figure 4). The air above
205 the Denver/Boulder area contained relatively diminished AOD (0.12, averaged from the domain of 39.5°N, 104.5°W,
206 40.5°N, and 105.5°W). Although the core of the plume remained north of Colorado, its more diffuse southern region
207 drifted south-eastward on 16 Aug. By 17 Aug, enhanced AOD was observed along the Front Range in northcentral
208 Colorado near Denver/Boulder (0.37). The AOD slightly decreased on 18 Aug over Denver/Boulder (0.25), which is
209 supported by the decrease of PM starting on 18 Aug from the CDPHE data (Figure 3). AOD increased in value and
210 spatial extent on 20 Aug during the second haze event, when more fires were detected in the Pacific Northwest (see



211 increase in number of MODIS hot spots in Figure 5). This plume contained a high density of aerosols travelled over
212 the northcentral U.S. The southern periphery of this plume impacted Colorado east of the Continental Divide starting
213 on 20 Aug, as corroborated by the CDPHE air quality measurements in Figure 3. Although the AOD values were not
214 as enhanced over Colorado as compared to the core of the AOD plume, AOD values over the Front Range were
215 enhanced as compared to before the long-range transport of this plume. Enhanced AOD was observed around
216 Denver/Boulder and the Front Range the following three days (0.26–0.35), with the largest values in this four-day
217 period observed on 23 Aug. The third haze event (Figure 6) followed a similar evolution to the first two. The AOD
218 plume remained north of Colorado on 26–27 Aug, then infiltrated the northern and eastern part of the state on 28–29
219 Aug. The AOD values over Denver/Boulder during this event (0.26–0.45) were considerably larger than the two
220 previous events. It is important to note that AOD is a column measurement, thus the largest aerosol concentrations
221 may be elevated in the atmosphere as compared to what is observed on the ground. However, the AOD observations
222 still provide information regarding the spatial extent of the plume of aerosols emitted from the fires and that Colorado
223 was indeed impacted by air transported from the Pacific Northwest fires.

224

225 Further, the satellite retrievals generally corroborate the air quality observations on the ground along the Front Range
226 in terms of when large concentrations of aerosols might be expected. More fires were detected across the Pacific
227 Northwest by MODIS during the second event (678 fires, on average) when $PM_{2.5}$ was largest as compared to the first
228 event (231 fires, on average), which had the smallest maximum $PM_{2.5}$ out of the three haze events. The third event
229 had $PM_{2.5}$ values in between the first and second, while also having 607 fires on average. Thus, the number of fires
230 likely influenced the relative amount of smoke produced and transported to the Front Range. However, meteorological
231 conditions as described below also played a vital role in enabling transport of the smoke.

232 3.3 Synoptic and regional scale meteorology fuel long-range aerosol transport from the Pacific Northwest

233 The transport of the enhanced AOD plume from the Pacific Northwest to Colorado during each of the three events,
234 and the relationship between the AOD column and ground-based in situ observations, are supported by the
235 meteorological features present on both the synoptic and regional scales. Plan-view synoptic analyses aloft and at the
236 surface during the first air quality event along Colorado's Front Range on 17–18 Aug 2015 are shown in Figure 7. At
237 500 hPa (Figure 7a and c), a transient shortwave trough embedded in baroclinic zonal flow aloft migrates eastward
238 across the northern Rocky Mountains (i.e., north of Colorado), with westerly (north-westerly) flow preceding
239 (following) the passage of the trough axis. These flow patterns are corroborated by the HYSPLIT air mass back
240 trajectories during the first event, shown in Figure 8a. At the surface, high pressure and shallow cool air initially
241 resides primarily north of Colorado at 0600 UTC 17 Aug (Figure 7b). However, by 2100 UTC 17 Aug (Figure 7d),
242 the shallow cool air has moved southward across eastern Colorado. A companion time-height section of hourly wind
243 profiles at BAO (Figure 9) shows low-level southerly flow ahead of the frontal passage at ~1100 UTC 17 Aug and
244 generally west to northwest flow aloft for the duration of the plot. The observed flow aloft is represented in many of
245 the back trajectories, which show west to northwest flow reaching Boulder during this event. Following the frontal
246 passage at the wind profiler, the shallow cool air mass deepens to ~3 km MSL by 1800 UTC 17 Aug in generally



247 northerly-component flow. Thereafter, the depth of the cool air decreases as the low-level flow shifts to south-easterly.
248 Operational rawinsonde data from Denver (not shown) captures the top of the frontal inversion at 2.1 km MSL at 1200
249 UTC 17 Aug and at 2.7 km MSL at 0000 UTC 18 Aug, consistent with the wind-profiler analysis of the time-varying
250 frontal altitude at BAO. For plan-view context, the times of the synoptic analyses are marked on the time-height
251 section. The large $PM_{2.5}$ values (Figure 3) on 17 Aug are corroborated by the transition of air arriving from enhanced
252 AOD regions (see air mass backward trajectories in Figure 8a) over and off the coast of the Pacific Northwest and
253 northern California (Figure 4c). $PM_{2.5}$ increased markedly after the passage of the shallow front, thus suggesting the
254 post-frontal air mass—which originated over Wyoming downstream of the Pacific Northwest fires—contains a large
255 concentration of particulates from those fires.

256

257 The evolution of the shallow cold front described above is typical of southward propagating cold fronts more generally
258 across eastern Colorado, and the frontal propagation is influenced heavily by the complex regional topography
259 depicted in Figure 1. Specifically, the blocking effect of the Rocky Mountains accelerates cold air southward along
260 the eastern side of the high terrain (e.g., Colle and Mass, 1995; Neiman et al., 2001). Additionally, the postfrontal
261 northerly-component airstream flowing across the west-east-oriented Cheyenne Ridge in south eastern Wyoming
262 induces an anticyclonic gyre to the lee (south) of this ridge, subsequently shifting the postfrontal flow from northerly
263 to easterly and driving the front westward against Colorado's Front Range (e.g., Davis, 1997; Neiman et al., 2001).

264

265 The meteorology during the second air quality event, on 22-23 Aug (Figure 10), is qualitatively similar to its
266 predecessor, although the transient shortwave trough aloft is more amplified during the latter event (Figure 10a and
267 c). Consequently, during the second event, the terrain-trapped cold front and its trailing shallow cool air mass east of
268 the Rockies surges much farther southward across eastern New Mexico (Figure 10b and d). The corresponding air
269 mass back trajectories (Figure 8b) travel south-eastward from the Pacific Northwest fires to Colorado. The wind-
270 profiler analysis at BAO (Figure 11) shows an abrupt low-level wind shift from westerly to easterly with the frontal
271 passage at 1900 UTC 22 Aug, followed by a rapid deepening of the shallow cool air mass to nearly 3 km MSL.
272 Thereafter, the depth of this air mass ranges between ~2.2 and 3.4 km MSL. Nearby rawinsonde observations at
273 Denver from 0000 UTC 23 Aug to 0000 UTC 24 Aug (not shown) document a strong frontal inversion ranging
274 between 3.3 and 3.8 km MSL, consistent with the wind-profiler analysis. Above the shallow cool air mass, the profiler
275 shows westerly flow aloft, shifting to north-westerly with the passage of the transient shortwave trough. The largest
276 $PM_{2.5}$ values observed during this event, on 23 Aug, corresponds to the most direct transport of air (Figure 8b) from
277 over the enhanced AOD regions over the Pacific Northwest fires (Figure 5). As with the previous case, the $PM_{2.5}$
278 increased markedly with the passage of the shallow front (Figure 3). Significantly, air quality is considerably poorer
279 with the second event, perhaps due partly to a stronger cold-frontal push across Colorado's Front Range that originated
280 near the smoky source region and partly due to north-westerly (rather than westerly) flow aloft that could transport
281 the smoke through a deeper layer toward Colorado. Further, more fires were detected during the second event (678,
282 on average) compared to the first event (231 fires, on average), thus the larger number of fires could result in more
283 smoke production and thus a denser smoke plume transported to the Front Range.



284

285 The synoptic-scale conditions on 27–28 Aug (Figure 12) associated with the third air quality case differ significantly
286 from those of the two earlier events. Most significantly, a broad ridge aloft covers the intermountain West for the
287 duration of this final event, while an embedded weak shortwave trough migrates eastward through the ridge from
288 Wyoming/Colorado to the Great Plains (Figure 12a and c). A surface reflection of the upper-level shortwave trough
289 is manifest as a weak low-pressure centre over western Nebraska and Kansas at 1800 UTC 27 Aug (Figure 12b). This
290 low migrates eastward during the subsequent 24 h (Figure 12d) in tandem with the upper-level shortwave. Because
291 this surface low resides beneath a mean ridge aloft, the temperature contrast across this trailing cold front is weaker
292 than its earlier counterparts (not shown). Nevertheless, the southward migration of the front east of the Rockies
293 suggests that terrain blocking may have influenced its evolution. The air mass back trajectories show parcels
294 originating from the region of the fires, similar to the trajectories from the earlier two events. Companion observations
295 from the BAO wind profiler (Figure 13) capture the shallow frontal passage at 2000 UTC 27 Aug, when westerly flow
296 shifts abruptly to northerly. Above 3 km MSL, the wind field exhibits a more gradual transition from westerly to
297 north-westerly as the weak shortwave trough moves across the wind profiler. The Denver rawinsondes at 0000 and
298 1200 UTC 28 Aug observed a frontal inversion at ~2.1 km MSL (not shown). It is less prominent than the frontal
299 inversions during the earlier events, largely because the temperature contrast across this front is weaker than its
300 predecessors. The subsequent rawinsonde profile at 0000 UTC 29 Aug (not shown) captures a deep, dry-convective
301 boundary layer extending up to 4 km MSL, despite persistent low-level northerly flow. Sensible heating eroded the
302 remnant low-level cool air east of the Rockies. $PM_{2.5}$ increases following the initial shallow cold-frontal passage at
303 2000 UTC 27 Aug and continues to increase for the remainder of the wind-profiler time-height section, as deep
304 northerly-component flow behind the weak shortwave trough transports smoke particulates across Colorado.

305 **3.4 Mineral dust and smoke arrive along the Front Range**

306 The types of aerosols present in the enhanced AOD plumes that were transported towards the Front Range via the
307 aforementioned synoptic conditions were evaluated using additional satellite-based measurements and support the
308 interpretation of transport of aerosols from the wildfires in the Pacific Northwest to Colorado. Figures 14–16 show
309 aerosol subtype data from the CALIPSO satellite in planar (a panels) and vertical-profile (b panels) views. Only on
310 the day prior to, or on the worst day of, each haze event are shown, although aerosol subtype data were examined
311 anytime CALIPSO passed over the Pacific Northwest or Colorado from 15 Aug to 2 Sep. CALIPSO demonstrates the
312 presence of smoke, dust, or polluted dust (dust mixed with smoke in each profile) during times that intersect the
313 enhanced AOD plume propagating from the Pacific Northwest or when over Colorado. Dust and smoke plumes from
314 the fires extended up to 10 km MSL over the western U.S. The mineral dust and smoke detected by CALIPSO in
315 transit to the Front Range was also detected with the TOPAZ lidar and the in situ aerosol particle mass and speciation
316 monitor at the DSRC. Figure 17 shows aerosol extinction profiles from the surface to 2.5 km AGL measured with the
317 TOPAZ lidar on 9 days during the smoke episodes. The time resolution of the extinction profiles is 5 minutes and the
318 vertical resolution is 1 m at the lowest altitudes, increasing to 6 m above 500 m AGL. The observations on 14 Aug
319 and 2 Sep, which bracket the smoke episodes, indicate very clean conditions with AOD from the surface up to 2.5 km



320 AGL ($AOD_{2.5km}$) of 0.05 and 0.04, respectively. Aerosol extinction coefficients and $AOD_{2.5km}$ were significantly
321 larger during the smoke episodes with an approximately 7-fold increase in $AOD_{2.5km}$ on 20 and 21 Aug. Aerosol
322 extinction was enhanced over the entire 2.5 km column, but the largest aerosol extinction values were observed in the
323 boundary layer in the lowest few hundred meters up to 1.5 km AGL. Also, the lidar measurements reveal that on most
324 days aerosol extinction varied significantly over the course of the day (e.g. 20 Aug). The largest aerosol extinction
325 values around 1–1.5 km AGL observed on 19 Aug were primarily due to swelling of aerosol particles in the moist
326 relative humidity environment beneath cumulus clouds at the top of the boundary layer. However, aerosol extinction
327 in the lower part of the boundary was still significantly larger than on 14 Aug, which is consistent with the larger
328 aerosol particle concentrations in the smoke plumes. The lidar measurements are consistent with the in situ $PM_{2.5}$ and
329 MODIS AOD observations. When comparing lidar $AOD_{2.5km}$ with MODIS AOD one has to be cognizant of the fact
330 that the TOPAZ observations only cover a portion of the atmospheric column and that the two AOD measurements
331 were made at different wavelengths.

332

333 Figure 18 shows the time series of $PM_{2.5}$, soil mass concentrations, and elemental mass concentrations (data from the
334 PX-375 was not available prior to this time period due to instrumental complications). Soil concentrations were
335 calculated by following the Interagency Monitoring of Protected Visual Environments (IMPROVE) convention using
336 concentrations of specific metals: $SOIL = 2.2[Al] + 2.49[Si] + 1.63[Ca] + 2.42[Fe] + 1.94[Ti]$ (Malm et al., 1994;
337 Hand et al., 2011). Both $PM_{2.5}$ and soil mass concentrations increased during the worst haze event days (i.e., 26 and
338 29 Aug), when the Pacific Northwest fires were influencing air along the Front Range and when CALIPSO showed
339 the presence of smoke and dust over the western U.S. The diurnal pattern is likely caused by the upslope/downslope
340 flow patterns due to proximity from the base of the foothills, which is particularly pronounced in the summer (Toth
341 and Johnson, 1985). Further, select metals also increased in concentrations during haze events, particularly those
342 typically sourced from mineral dust (i.e., in the IMPROVE soil convention equation) and S and K, which are metal
343 tracers that have been observed in smoke or biomass burning aerosols originating from fires (Artaxo et al., 1994;
344 Gaudichet et al., 1995; Yamasoe et al., 2000; Pachon et al., 2013).

345

346 Figure 19 shows the average concentrations of mineral dust or biomass burning metal tracers from the PX-375 from
347 26 Aug to 2 Sep, during conditions influenced by the Pacific Northwest fires (days with enhanced $PM_{2.5}$; 29–30 Aug)
348 and days with cleaner, normal Front Range conditions (days with small $PM_{2.5}$; remaining days during this time period).
349 $PM_{2.5}$ and soil mass, biomass burning metals (S and K), and mineral dust marker (Al, Si, Fe, and Ca) concentrations
350 were all larger, on average, during influences from the Pacific Northwest fires, corroborating the CALIPSO
351 observations. Also included are metals that are typical of industrial tracers As and Pb (Figure 19e) (Paciga and Jervis,
352 1976; Hutton and Symon, 1986; Thomaidis et al., 2003), which were actually smaller during influences from wildfires
353 and larger during normal, regionally-sourced influences. The average $PM_{2.5}$ mass concentration from the CDPHE data
354 was almost 3 times larger on 29–30 Aug as compared to the remaining days in the 26 Aug–2 Sep time period (15.9
355 versus $5.7 \mu g m^{-3}$, respectively). This result demonstrates how influences from typical, regional industrial sources is
356 disrupted by the synoptic conditions that introduced the long-range transported biomass burning plumes. Although Zn



357 and Cu have been shown to originate from wildfires (Yamasoe et al., 2000), the averages were similar—within 1 ng
358 m⁻³—thus a distinct comparison could not be made within certainty. Further, these metals can also be derived from
359 vehicular emissions, thus their concentrations may additionally be influenced by local traffic (Sternbeck et al., 2002).
360 These results demonstrate the transport of mineral dust and biomass burning aerosol species to the Front Range, which
361 were indeed larger in concentration during poor air quality/haze events. Interestingly, mineral dust mixed within a
362 smoke plume from fires has predominantly been observed originating from more arid regions along the global dust
363 belt, and using modelling or remote sensing data only (e.g., Radojevic, 2003; Tesche et al., 2009; Yang et al., 2013;
364 Nisantzi et al., 2014). To our knowledge, this co-lofting of dust and smoke has not been shown to occur in the U.S.,
365 particularly in a region as densely covered in vegetation as the Pacific Northwest.

366 **4 Conclusions**

367 We have demonstrated the transport of large quantities of mineral dust and smoke/biomass burning aerosols from
368 wildfires in the Pacific Northwest to the Colorado Front Range. These aerosols were transported under synoptic
369 conditions that contributed to three different haze events, inducing poor air quality in the Denver metro area. Three
370 separate poor air quality events with enhanced PM_{2.5} were likely dependent on the number of fires and observed to
371 occur with cold frontal passages along Colorado's Front Range, enabling the enhanced AOD plumes originating from
372 the Pacific Northwest wildfires to propagate south-eastward to Colorado's Front Range. Air masses were shown to
373 originate from over the region dense with wildfires, and followed through satellite-detected aerosol plumes, which
374 were rich in a mixture of mineral dust and smoke. Tracers for these aerosol types were also detected in situ along the
375 Front Range, and were shown to be enhanced during periods of influence from the fires.

376

377 Overall, these unique observations were demonstrated using a complete suite of in situ and remote sensing aerosol
378 measurements in the context of in situ meteorological observations and air mass trajectory modelling. In tandem, we
379 utilized a real-time X-ray fluorescence spectroscopy technique using the novel and field-portable PX-375 from
380 HORIBA, Ltd. demonstrating the utility of the instrument. Although the haze events were short lived, they
381 demonstrate how quickly aerosols can be transported long distances and affect air quality in regions thousands of
382 kilometres away. Interestingly, mineral dust was observed to be co-lofted and transported within the smoke plumes,
383 an observation not previously reported for vegetated regions such as the Pacific Northwest.

384

385 Mineral dust and smoke aerosols have disparate implications for health and climate (i.e., by serving as seeds for cloud
386 particle formation, which impacts cloud lifetime, radiative effects, and precipitation formation mechanisms),
387 particularly at the levels observed along the Front Range. These unique observations should be taken into account
388 when developing health standards, seeing as not only regional urban and industrial emissions contribute to poor air
389 quality conditions. Additionally, dust and smoke are efficient cloud forming nuclei, particularly when orographically
390 lifted along barriers such as the Front Range into the upper atmosphere, where cloud formation is prominent. Thus,
391 transport of these aerosols from wildfires has broad implications for altering aerosol composition in regions far from
392 the source.



393 **Author contribution.** J. M. C. analysed XRF data, compiled CDPHE and MODIS data, ran HYSPLIT simulations,
394 and wrote the manuscript. P. J. N. conducted meteorological analysis and interpretation. T. C. compiled and analysed
395 CALIPSO data. C. J. S., G. K., and R. A. analysed and supplied TOPAZ data. A. Y. provided PX-375 for usage. All
396 co-authors contributed to the writing of or provided comments for manuscript.

397 **Acknowledgements.** The authors would like to acknowledge the many agencies and organization from which data
398 were acquired, including the CDPHE for air quality data, NASA for MODIS and CALIPSO observations, NOAA for
399 HYSPLIT and HMT meteorological data, and the HDF group for providing example code to process CALIPSO data.

400 **References**

- 401 Ackerman, S. A., Strabala, K. I., Menzel, W. P., Frey, R. A., Moeller, C. C., and Gumley, L. E.: Discriminating clear sky from
402 clouds with MODIS, *J Geophys Res-Atmos*, 103, 32141-32157, 1998.
- 403 Alvarez, R. J., Senff, C. J., Langford, A. O., Weickmann, A. M., Law, D. C., Machol, J. L., Merritt, D. A., Marchbanks, R. D.,
404 Sandberg, S. P., Brewer, W. A., Hardesty, R. M., and Banta, R. M.: Development and Application of a Compact, Tunable,
405 Solid-State Airborne Ozone Lidar System for Boundary Layer Profiling, *J Atmos Ocean Tech*, 28, 1258-1272, 2011.
- 406 Alvarez, R. J., Senff, C. J., Weickmann, A. M., Sandberg, S. P., Langford, A. O., Marchbanks, R. D., Brewer, W. A., and Hardesty,
407 R. M.: Reconfiguration of the NOAA TOPAZ lidar for ground-based measurement of ozone and aerosol backscatter,
408 Proceedings of the 26th International Laser Radar Conference, Porto Heli, Greece, 2012,
- 409 Ansmann, A., Baars, H., Tesche, M., Muller, D., Althausen, D., Engelmann, R., Pauliquevis, T., and Artaxo, P.: Dust and smoke
410 transport from Africa to South America: Lidar profiling over Cape Verde and the Amazon rainforest, *Geophys Res Lett*,
411 36, 2009.
- 412 Artaxo, P., Gerab, F., Yamasoe, M. A., and Martins, J. V.: Fine Mode Aerosol Composition at 3 Long-Term Atmospheric
413 Monitoring Sites in the Amazon Basin, *J Geophys Res-Atmos*, 99, 22857-22868, 1994.
- 414 Baars, H., Ansmann, A., Althausen, D., Engelmann, R., Artaxo, P., Pauliquevis, T., and Souza, R.: Further evidence for significant
415 smoke transport from Africa to Amazonia, *Geophys Res Lett*, 38, 2011.
- 416 Benjamin, S. G., Weygandt, S. S., Brown, J. M., Hu, M., Alexander, C., Smirnova, T. G., Olson, J. B., James, E., Dowell, D. C.,
417 Grell, G. A., Lin, H., Peckham, S. E., Smith, T. L., and Moninger, W. R.: A North American hourly assimilation and
418 model forecast cycle: The rapid refresh, *Mon. Wea. Rev.*, 144, in review, 2016.
- 419 Bowman, D. J. S., and Johnston, F.: Wildfire Smoke, Fire Management, and Human Health, *EcoHealth*, 2, 76-80, 2005.
- 420 Bravo, A. H., Sosa, E. R., Sanchez, A. P., Jaimes, P. M., and Saavedra, R. M. I.: Impact of wildfires on the air quality of Mexico
421 City, 1992-1999, *Environ Pollut*, 117, 243-253, 2002.
- 422 Brown, S. S., Thornton, J. A., Keene, W. C., Pszenny, A. A. P., Sive, B. C., Dube, W. P., Wagner, N. L., Young, C. J., Riedel, T.
423 P., Roberts, J. M., VandenBoer, T. C., Bahreini, R., Ozturk, F., Middlebrook, A. M., Kim, S., Hubler, G., and Wolfe, D.
424 E.: Nitrogen, Aerosol Composition, and Halogens on a Tall Tower (NACHTT): Overview of a wintertime air chemistry
425 field study in the front range urban corridor of Colorado, *J Geophys Res-Atmos*, 118, 8067-8085, 2013.
- 426 Chalbot, M. C., Nikolich, G., Etyemezian, V., Dubois, D. W., King, J., Shafer, D., da Costa, G. G., Hinton, J. F., and Kavouras, I.
427 G.: Soil humic-like organic compounds in prescribed fire emissions using nuclear magnetic resonance spectroscopy,
428 *Environ Pollut*, 181, 167-171, 2013.



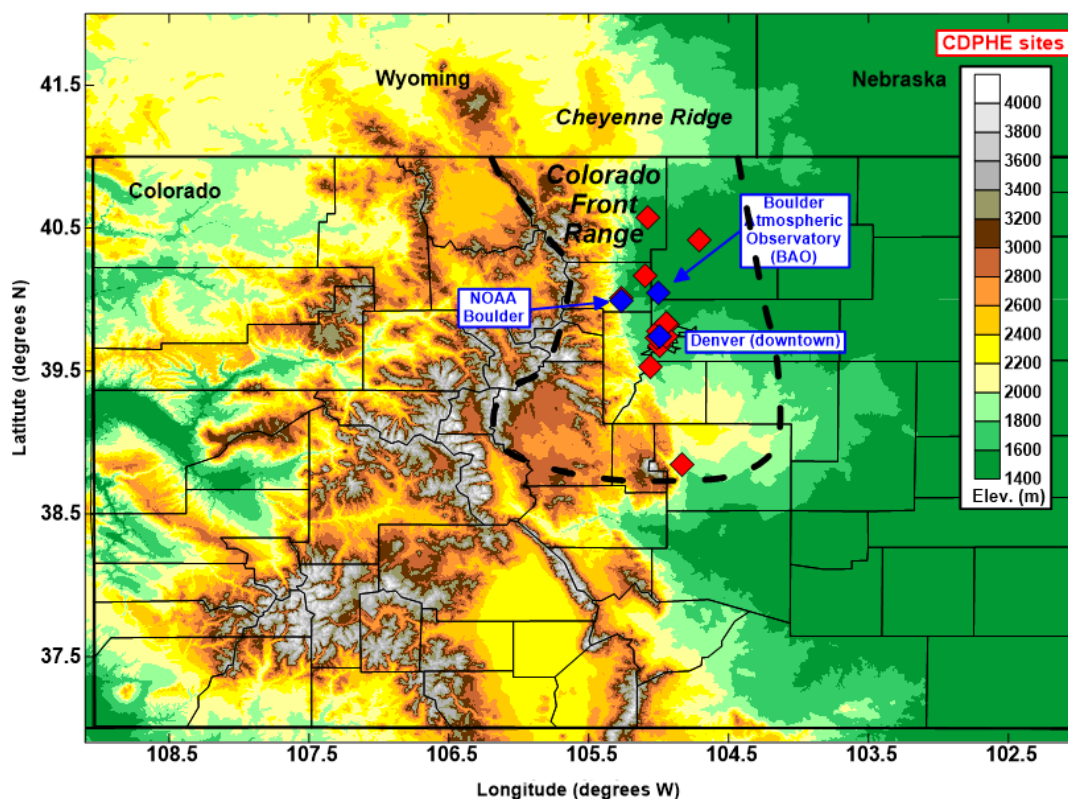
- 429 Clements, C. B., Zhong, S. Y., Bian, X. D., Heilman, W. E., and Byun, D. W.: First observations of turbulence generated by grass
430 fires, *J Geophys Res-Atmos*, 113, 2008.
- 431 Colle, B. A., and Mass, C. F.: The Structure and Evolution of Cold Surges East of the Rocky-Mountains, *Mon Weather Rev*, 123,
432 2577-2610, 1995.
- 433 Cruz, C. N., and Pandis, S. N.: A study of the ability of pure secondary organic aerosol to act as cloud condensation nuclei, *Atmos*
434 *Environ*, 31, 2205-2214, 1997.
- 435 Davis, C. A.: Mesoscale anticyclonic circulations in the Lee of the central Rocky Mountains, *Mon Weather Rev*, 125, 2838-2855,
436 1997.
- 437 DeMott, P. J., Chen, Y., Kreidenweis, S. M., Rogers, D. C., and Sherman, D. E.: Ice formation by black carbon particles, *Geophys*
438 *Res Lett*, 26, 2429-2432, 1999.
- 439 DeMott, P. J., Sassen, K., Poellot, M. R., Baumgardner, D., Rogers, D. C., Brooks, S. D., Prenni, A. J., and Kreidenweis, S. M.:
440 African dust aerosols as atmospheric ice nuclei, *Geophys Res Lett*, 30, 2003.
- 441 Draxler, R. R., and Rolph, G. D.: HYSPLIT (HYbrid Single-Particle Lagrangian Integrated Trajectory) Model access via NOAA
442 ARL READY Website (<http://ready.arl.noaa.gov/HYSPLIT.php>), 2011.
- 443 Eagan, R. C., Hobbs, P. V., and Radke, L. F.: Measurements of Cloud Condensation Nuclei and Cloud Droplet Size Distributions
444 in Vicinity of Forest Fires, *J Appl Meteorol*, 13, 553-557, 1974.
- 445 Gadi, R., Kulshrestha, U. C., Sarkar, A. K., Garg, S. C., and Parashar, D. C.: Emissions of SO₂ and NO_x from biofuels in India,
446 *Tellus B*, 55, 787-795, 2003.
- 447 Gaudichet, A., Echalar, F., Chatenet, B., Quisefit, J. P., Malingre, G., Cachier, H., Buatmenard, P., Artaxo, P., and Maenhaut, W.:
448 Trace-Elements in Tropical African Savanna Biomass Burning Aerosols, *J Atmos Chem*, 22, 19-39, 1995.
- 449 Giglio, L., Descloitres, J., Justice, C. O., and Kaufman, Y. J.: An enhanced contextual fire detection algorithm for MODIS, *Remote*
450 *Sens Environ*, 87, 273-282, 2003.
- 451 Giglio, L.: MODIS Collection 5 Active Fire Product User's Guide Version 2.4, Science Systems and Applications, Inc., 2010.
- 452 Haagenson, P. L.: Meteorological and Climatological Factors Affecting Denver Air-Quality, *Atmos Environ*, 13, 79-85, 1979.
- 453 Hand, J. L., Copland, S. A., Dillner, A. M., Indresand, H., Malm, W. C., McDade, C. E., Moore, C. T., Pitchford, M. L., Schichtel,
454 B. A., and Watson, J. G.: Spatial and Seasonal Patterns and Temporal Variability of Haze and its Constituents in the
455 United States Report V Cooperative Institute for Research in the Atmosphere, 2011.
- 456 Hutton, M., and Symon, C.: The Quantities of Cadmium, Lead, Mercury and Arsenic Entering the Uk Environment from Human
457 Activities, *Sci Total Environ*, 57, 129-150, 1986.
- 458 Jacob, D. J., and Winner, D. A.: Effect of climate change on air quality, *Atmos Environ*, 43, 51-63, 2009.
- 459 Jaffe, D. A., and Wigder, N. L.: Ozone production from wildfires: A critical review, *Atmos Environ*, 51, 1-10, 2012.
- 460 Jayachandran, S.: Air quality and early-life mortality: Evidence from Indonesia's wildfires, *J. Human Resources*, 44, 916-954,
461 2008.
- 462 Kalnay, E., Kanamitsu, M., Kistler, R., Collins, W., Deaven, D., Gandin, L., Iredell, M., Saha, S., White, G., Woollen, J., Zhu, Y.,
463 Chelliah, M., Ebisuzaki, W., Higgins, W., Janowiak, J., Mo, K. C., Ropelewski, C., Wang, J., Leetmaa, A., Reynolds,
464 R., Jenne, R., and Joseph, D.: The NCEP/NCAR 40-year reanalysis project, *B Am Meteorol Soc*, 77, 437-471, 1996.
- 465 Kaufman, Y. J., Tanre, D., Remer, L. A., Vermote, E. F., Chu, A., and Holben, B. N.: Operational remote sensing of tropospheric
466 aerosol over land from EOS moderate resolution imaging spectroradiometer, *J Geophys Res-Atmos*, 102, 17051-17067,
467 1997.
- 468 Liu, Y. Q., Stanturf, J., and Goodrick, S.: Trends in global wildfire potential in a changing climate, *Forest Ecol Manag*, 259, 685-
469 697, 2010.



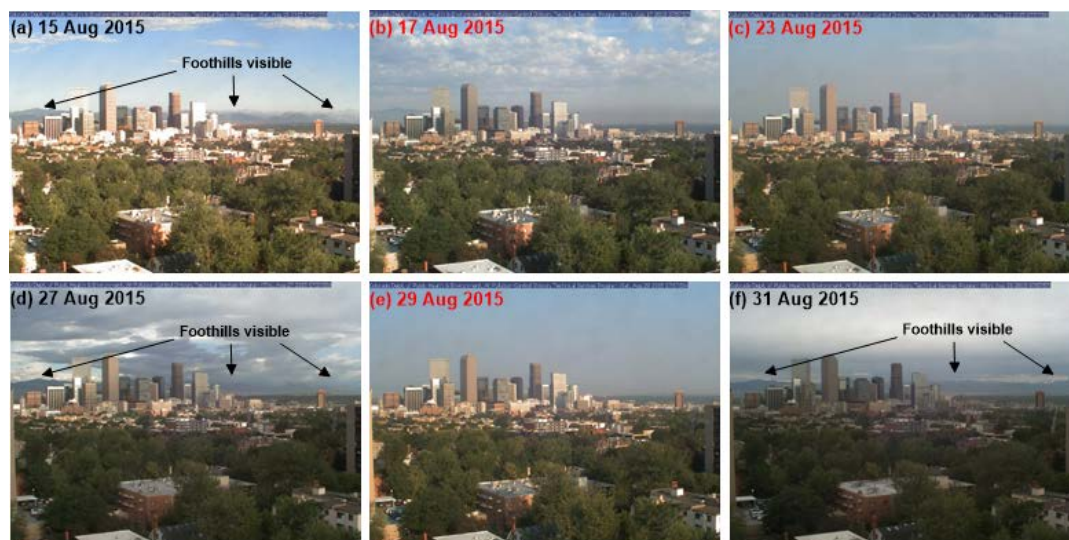
- 470 Malm, W. C., Sisler, J. F., Huffman, D., Eldred, R. A., and Cahill, T. A.: Spatial and Seasonal Trends in Particle Concentration
471 and Optical Extinction in the United-States, *J Geophys Res-Atmos*, 99, 1347-1370, 1994.
- 472 McCluskey, C. S., DeMott, P. J., Prenni, A. J., Levin, E. J. T., McMeeking, G. R., Sullivan, A. P., Hill, T. C. J., Nakao, S., Carrico,
473 C. M., and Kreidenweis, S. M.: Characteristics of atmospheric ice nucleating particles associated with biomass burning
474 in the US: Prescribed burns and wildfires, *J Geophys Res-Atmos*, 119, 2014.
- 475 Moore, D., Copes, R., Fisk, R., Joy, R., Chan, K., and Brauer, M.: Population Health Effects of Air Quality Changes Due to Forest
476 Fires in British Columbia in 2003: Estimates from Physician-visit Billing Data, *Canadian Journal of Public Health /*
477 *Revue Canadienne de Sante'e Publique*, 97, 105-108, 2006.
- 478 Mott, J. A., Meyer, P., Mannino, D., Redd, S. C., Smith, E. M., Gotway-Crawford, C., and Chase, E.: Wildland forest fire smoke:
479 health effects and intervention evaluation, Hoopa, California, 1999, *Western Journal of Medicine*, 176, 157-162, 2002.
- 480 Neff, J. C., Ballantyne, A. P., Farmer, G. L., Mahowald, N. M., Conroy, J. L., Landry, C. C., Overpeck, J. T., Painter, T. H.,
481 Lawrence, C. R., and Reynolds, R. L.: Increasing eolian dust deposition in the western United States linked to human
482 activity, *Nat Geosci*, 1, 189-195, 2008.
- 483 Neiman, P. J., Ralph, F. M., Weber, R. L., Uttal, T., Nance, L. B., and Levinson, D. H.: Observations of nonclassical frontal
484 propagation and frontally forced gravity waves adjacent to steep topography, *Mon Weather Rev*, 129, 2633-2659, 2001.
- 485 Nisantzi, A., Mamouri, R. E., Ansmann, A., and Hadjimitsis, D.: Injection of mineral dust into the free troposphere during fire
486 events observed with polarization lidar at Limassol, Cyprus, *Atmos Chem Phys*, 14, 12155-12165, 2014.
- 487 Nriagu, J. O.: A Global Assessment of Natural Sources of Atmospheric Trace-Metals, *Nature*, 338, 47-49, 1989.
- 488 Omar, A. H., Winker, D. M., Kittaka, C., Vaughan, M. A., Liu, Z. Y., Hu, Y. X., Trepte, C. R., Rogers, R. R., Ferrare, R. A., Lee,
489 K. P., Kuehn, R. E., and Hostetler, C. A.: The CALIPSO Automated Aerosol Classification and Lidar Ratio Selection
490 Algorithm, *J Atmos Ocean Tech*, 26, 1994-2014, 2009.
- 491 Pachon, J. E., Weber, R. J., Zhang, X. L., Mulholland, J. A., and Russell, A. G.: Revising the use of potassium (K) in the source
492 apportionment of PM_{2.5}, *Atmos Pollut Res*, 4, 14-21, 2013.
- 493 Paciga, J. J., and Jervis, R. E.: Multielement Size Characterization of Urban Aerosols, *Environ Sci Technol*, 10, 1124-1128, 1976.
- 494 Park, R. J., Jacob, D. J., Chin, M., and Martin, R. V.: Sources of carbonaceous aerosols over the United States and implications for
495 natural visibility, *J Geophys Res-Atmos*, 108, 2003.
- 496 Phuleria, H. C., Fine, P. M., Zhu, Y. F., and Sioutas, C.: Air quality impacts of the October 2003 Southern California wildfires, *J*
497 *Geophys Res-Atmos*, 110, 2005.
- 498 Pinker, R. T., Liu, H., Osborne, S. R., and Akoshile, C.: Radiative effects of aerosols in sub-Sahel Africa: Dust and biomass burning,
499 *J Geophys Res-Atmos*, 115, 2010.
- 500 Pio, C. A., Legrand, M., Alves, C. A., Oliveira, T., Afonso, J., Caseiro, A., Puxbaum, H., Sanchez-Ochoa, A., and Gelencser, A.:
501 Chemical composition of atmospheric aerosols during the 2003 summer intense forest fire period, *Atmos Environ*, 42,
502 7530-7543, 2008.
- 503 Radojevic, M.: Chemistry of forest fires and regional haze with emphasis on Southeast Asia, *Pure Appl Geophys*, 160, 157-187,
504 2003.
- 505 Sibold, J. S., and Veblen, T. T.: Relationships of subalpine forest fires in the Colorado Front Range with interannual and
506 multidecadal-scale climatic variation, *J Biogeogr*, 33, 833-842, 2006.
- 507 Spracklen, D. V., Logan, J. A., Mickley, L. J., Park, R. J., Yevich, R., Westerling, A. L., and Jaffe, D. A.: Wildfires drive interannual
508 variability of organic carbon aerosol in the western US in summer, *Geophys Res Lett*, 34, 2007.
- 509 Sternbeck, J., Sjodin, A., and Andreasson, K.: Metal emissions from road traffic and the influence of resuspension - results from
510 two tunnel studies, *Atmos Environ*, 36, 4735-4744, 2002.



- 511 Streets, D. G., Yarber, K. F., Woo, J. H., and Carmichael, G. R.: Biomass burning in Asia: Annual and seasonal estimates and
512 atmospheric emissions, *Global Biogeochem Cy*, 17, 2003.
- 513 Tesche, M., Ansmann, A., Müller, D., Althausen, D., Engelmann, R., Freudenthaler, V., and Gross, S.: Vertically resolved
514 separation of dust and smoke over Cape Verde using multiwavelength Raman and polarization lidars during Saharan
515 Mineral Dust Experiment 2008, *J Geophys Res-Atmos*, 114, 2009.
- 516 Thomaidis, N. S., Bakeas, E. B., and Siskos, P. A.: Characterization of lead, cadmium, arsenic and nickel in PM_{2.5} particles in the
517 Athens atmosphere, Greece, *Chemosphere*, 52, 959-966, 2003.
- 518 Toth, J. J., and Johnson, R. H.: Summer Surface Flow Characteristics over Northeast Colorado, *Mon Weather Rev*, 113, 1458-
519 1469, 1985.
- 520 Vali, G., DeMott, P. J., Mohler, O., and Whale, T. F.: Technical Note: A proposal for ice nucleation terminology, *Atmos Chem
521 Phys*, 15, 10263-10270, 2015.
- 522 VanCuren, R. A.: Asian aerosols in North America: Extracting the chemical composition and mass concentration of the Asian
523 continental aerosol plume from long-term aerosol records in the western United States, *J Geophys Res-Atmos*, 108, 2003.
- 524 Vaughan, M., Young, S., Winker, D., Powell, K., Omar, A., Liu, Z. Y., Hu, Y. X., and Hostetler, C.: Fully automated analysis of
525 space-based lidar data: an overview of the CALIPSO retrieval algorithms and data products, *Bba Lib*, 5575, 16-30, 2004.
- 526 Watson, J. G., Fujita, E., Chow, J. C., Zielinska, B., Richards, L. W., Neff, W., and Dietrich, D.: Northern Front Range Air Quality
527 Study Final Report, 1998.
- 528 Weber, B. L., Wuertz, D. B., and Welsh, D. C.: Quality Controls for Profiler Measurements of Winds and RASS Temperatures, *J
529 Atmos Ocean Tech*, 10, 452-464, 1993.
- 530 Westerling, A. L., Hidalgo, H. G., Cayan, D. R., and Swetnam, T. W.: Warming and earlier spring increase western US forest
531 wildfire activity, *Science*, 313, 940-943, 2006.
- 532 White, A. B., Anderson, M. L., Dettinger, M. D., Ralph, F. M., Hinojosa, A., Cayan, D. R., Hartman, R. K., Reynolds, D. W.,
533 Johnson, L. E., Schneider, T. L., Cifelli, R., Toth, Z., Gutman, S. I., King, C. W., Gehrke, F., Johnston, P. E., Walls, C.,
534 Mann, D., Gottas, D. J., and Coleman, T.: A Twenty-First-Century California Observing Network for Monitoring
535 Extreme Weather Events, *J Atmos Ocean Tech*, 30, 1585-1603, 2013.
- 536 Wiedinmyer, C., Quayle, B., Geron, C., Belote, A., McKenzie, D., Zhang, X. Y., O'Neill, S., and Wynne, K. K.: Estimating
537 emissions from fires in North America for air quality modeling, *Atmos Environ*, 40, 3419-3432, 2006.
- 538 Winker, D. M., Vaughan, M. A., Omar, A., Hu, Y. X., Powell, K. A., Liu, Z. Y., Hunt, W. H., and Young, S. A.: Overview of the
539 CALIPSO Mission and CALIOP Data Processing Algorithms, *J Atmos Ocean Tech*, 26, 2310-2323, 2009.
- 540 Yamasoe, M. A., Artaxo, P., Miguel, A. H., and Allen, A. G.: Chemical composition of aerosol particles from direct emissions of
541 vegetation fires in the Amazon Basin: water-soluble species and trace elements, *Atmos Environ*, 34, 1641-1653, 2000.
- 542 Yang, Z. F., Wang, J., Ichoku, C., Hyer, E., and Zeng, J.: Mesoscale modeling and satellite observation of transport and mixing of
543 smoke and dust particles over northern sub-Saharan African region, *J Geophys Res-Atmos*, 118, 12139-12157, 2013.
- 544 Zamora, R. J., Dutton, E. G., Trainer, M., McKeen, S. A., Wilczak, J. M., and Hou, Y. T.: The accuracy of solar irradiance
545 calculations used in mesoscale numerical weather prediction, *Mon Weather Rev*, 133, 783-792, 2005.
- 546



547
548 **Figure 1.** Map of monitoring locations, including NOAA DSRC in Boulder, which housed the PX-375 and
549 TOPAZ lidar instruments, the BAO where the 449-MHz wind profiler was deployed, downtown Denver, and
550 the CDPHE sites where $PM_{2.5}$ and PM_{10} are monitored (see Table 1 for site descriptions). The approximate
551 area encompassing the Colorado Front Range is highlighted by the dashed line. The Cheyenne Ridge in
552 Wyoming is also notated.



553

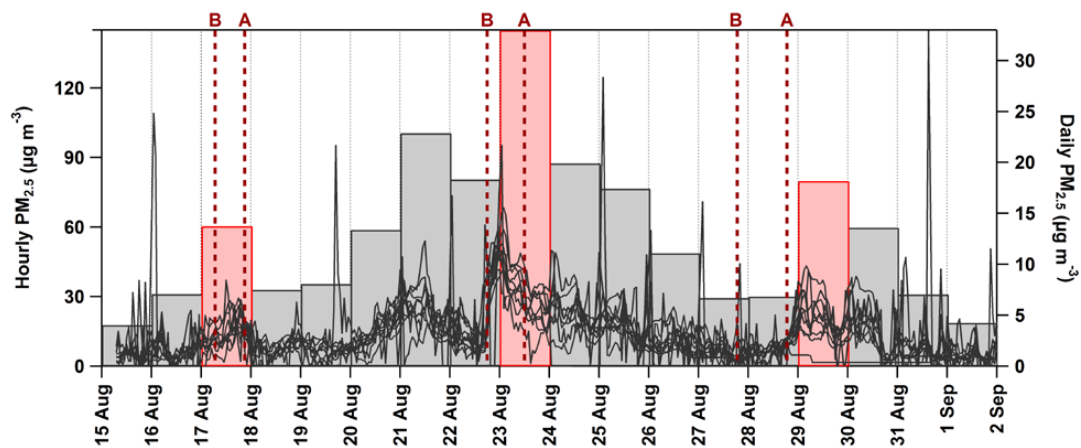
554

555

556

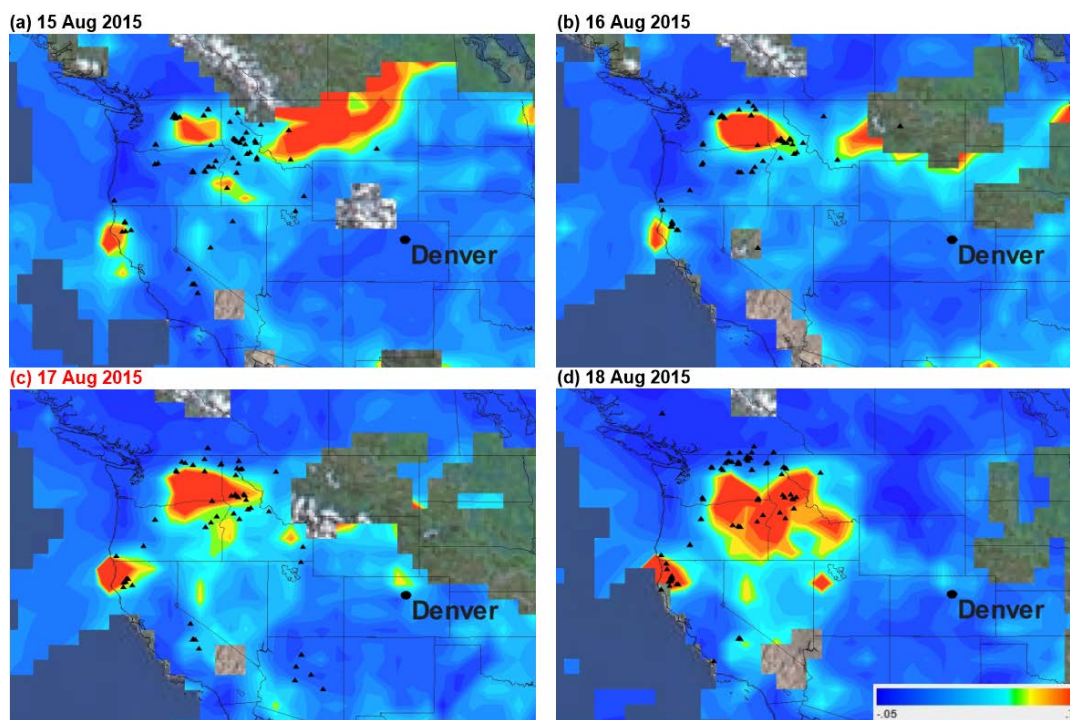
557

Figure 2. Images of downtown Denver facing west taken at 1400 UTC (0800 MDT). Images acquired from the CDPHE Visibility Station (DESCI; 39.73°N, 104.96°W; 1633 m MSL). Only days of significant meteorological and visibility transitions in August 2015 are shown. Days in red are those which correspond to the haziest days during the study time period. In panels (a), (d), and (f), the visibility of the foothills (and background high terrain) is highlighted.



558

559 **Figure 3. Hourly and daily averaged PM_{2.5} mass concentrations at CDPHE sites. The pairs of red dashed lines**
560 **shows the times before “B” and after “A” cold-frontal passages at BAO during or prior to each haze event. The**
561 **daily averaged PM_{2.5} in red represent the haziest days during or following cold frontal passages (i.e., Events**
562 **1, 2, and 3 on 17, 23, and 29 Aug 2015, respectively).**



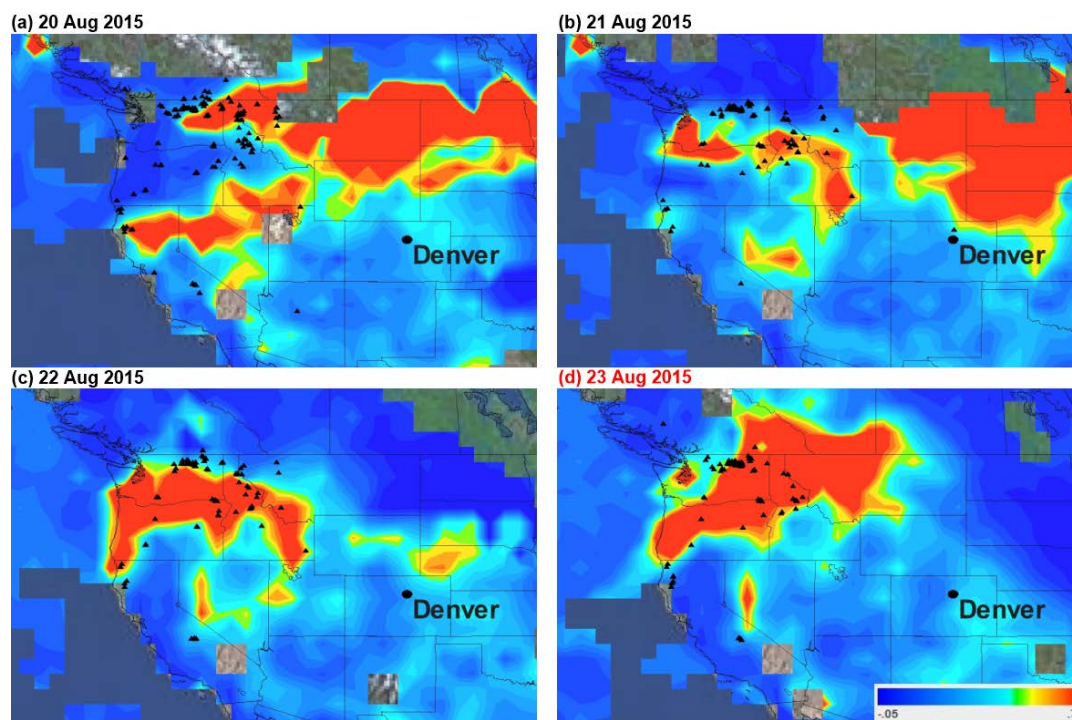
563

564

565

566

Figure 4. Daily averaged aerosol optical depth (AOD; colour bar lower right) and fire hotspots (black markers) detected by MODIS during the first major haze case study between 15 and 18 Aug 2015. The haziest day from the CDPHE data is labelled in red (i.e., Event 1).

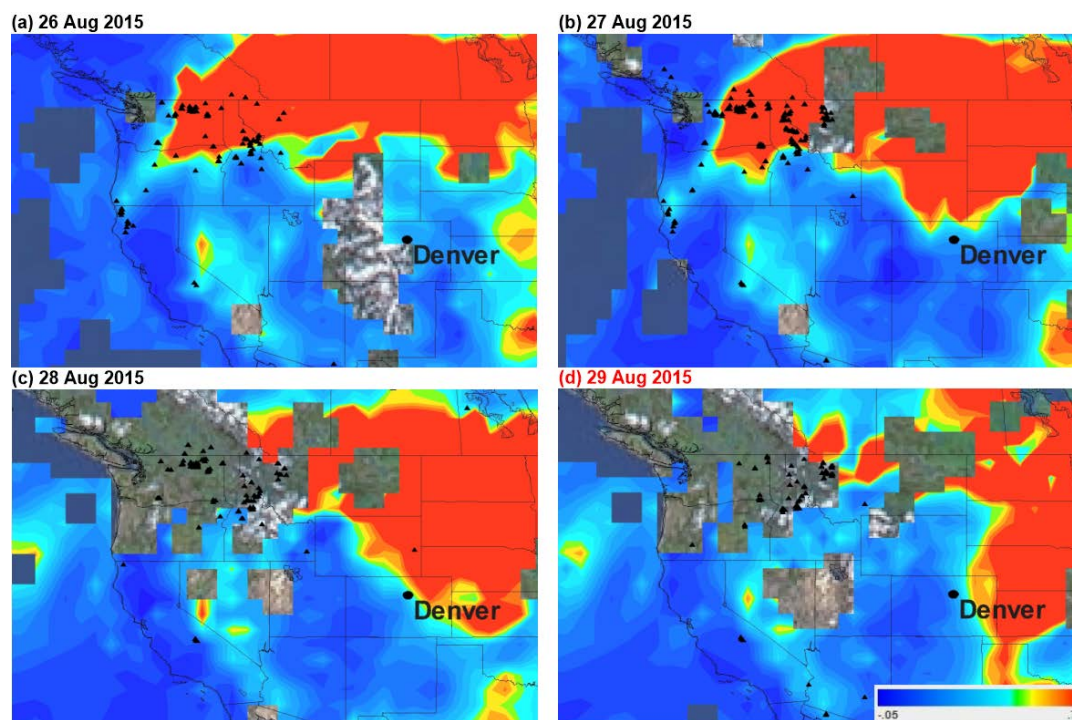


567

568

569

Figure 5. Same as Figure 4, but for the second major haze event between 20 and 23 Aug 2015. The haziest day from the CDPHE data is labelled in red (i.e., Event 2).

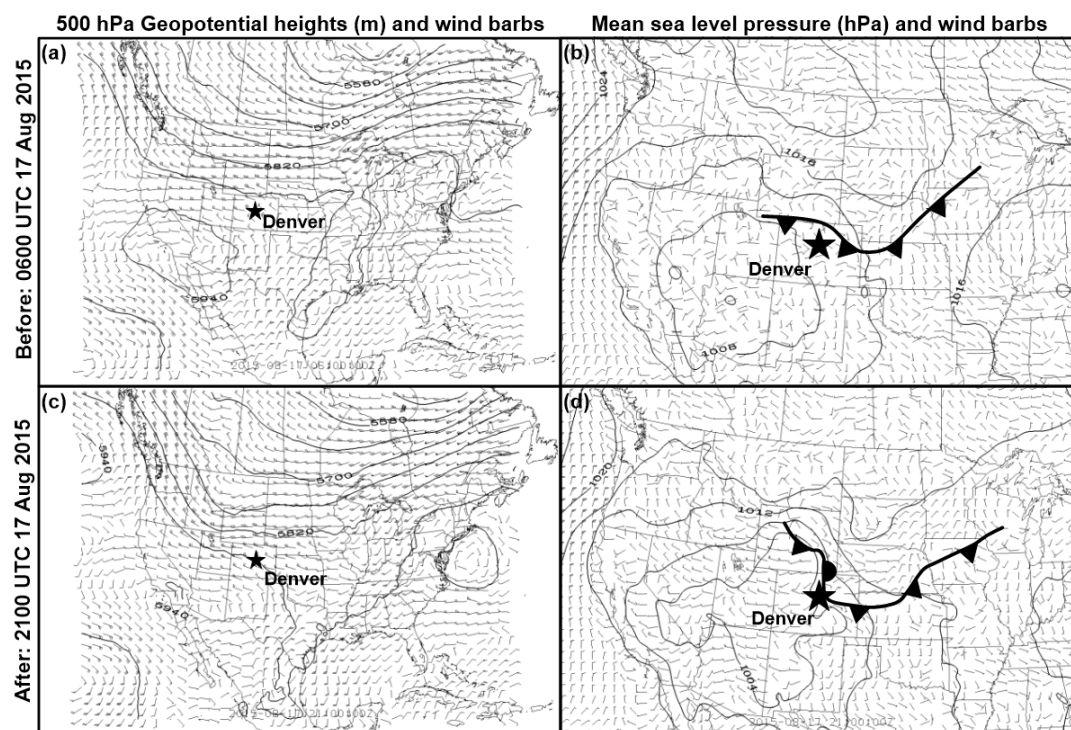


570

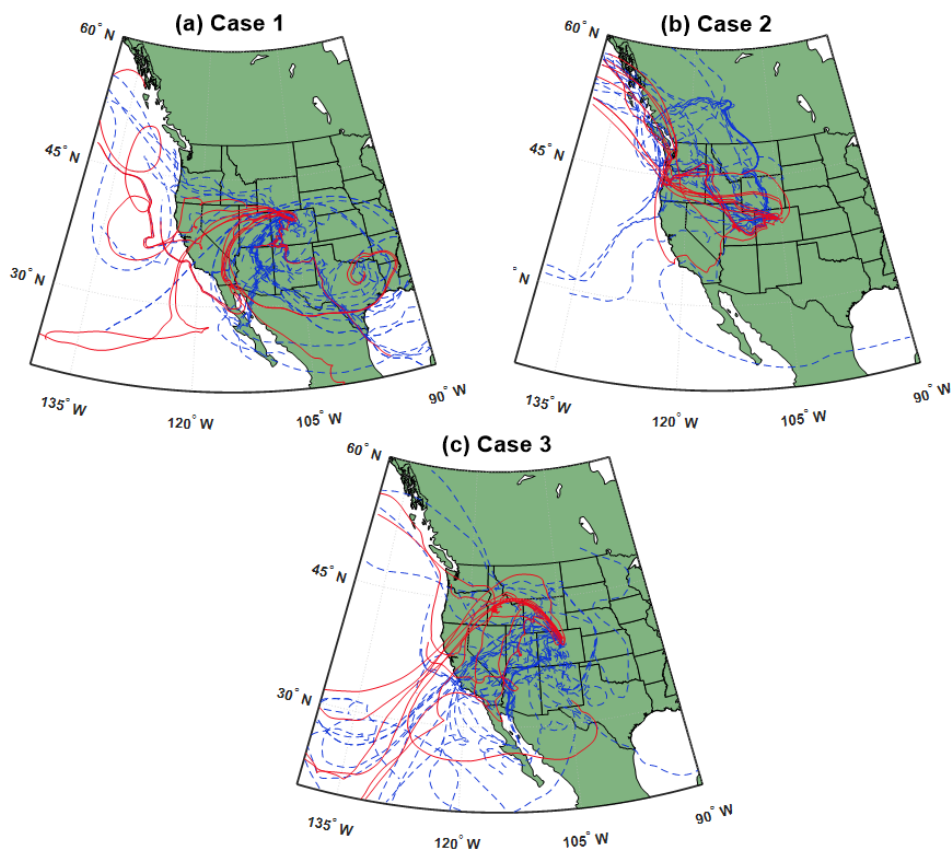
571

572

Figure 6. Same as Figure 4, but for the third major haze event between 26 and 29 Aug 2015. The haziest day from the CDPHE data is labelled in red (i.e., Event 3).

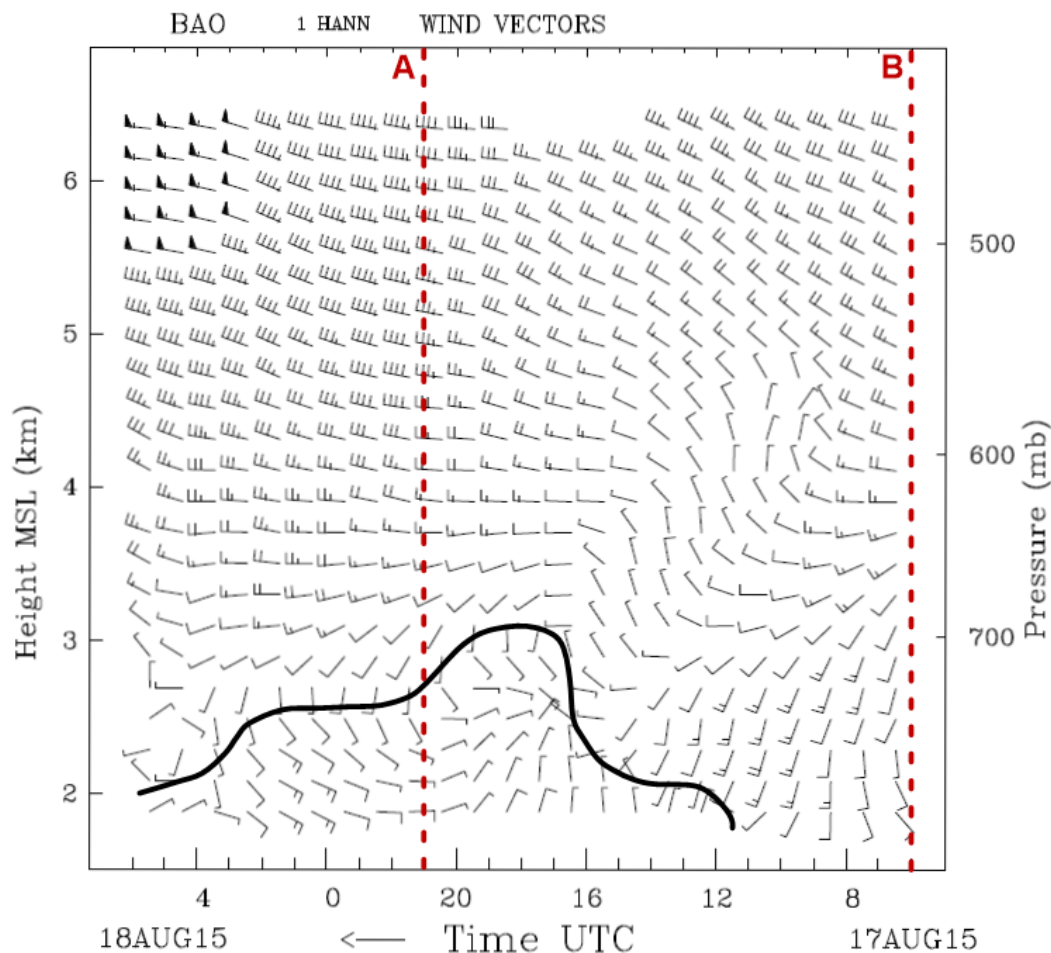


573
574 **Figure 7.** Plan-view analyses from before and after the passage of a cold front during Event 1: 0600 and 2100 UTC 17 Aug
575 2015, respectively. Analyses include the 13-km resolution RAP gridded dataset of (left column) 500-hPa geopotential heights
576 (m, black contours) with 500-hPa wind velocities (flags = 25 m s^{-1} , barbs = 5 m s^{-1} , half-barbs = 2.5 m s^{-1}) and (right column)
577 mean sea-level pressure (mb, black contours) with near-surface wind velocities (flags and barbs as above). Standard frontal
578 notation is used.



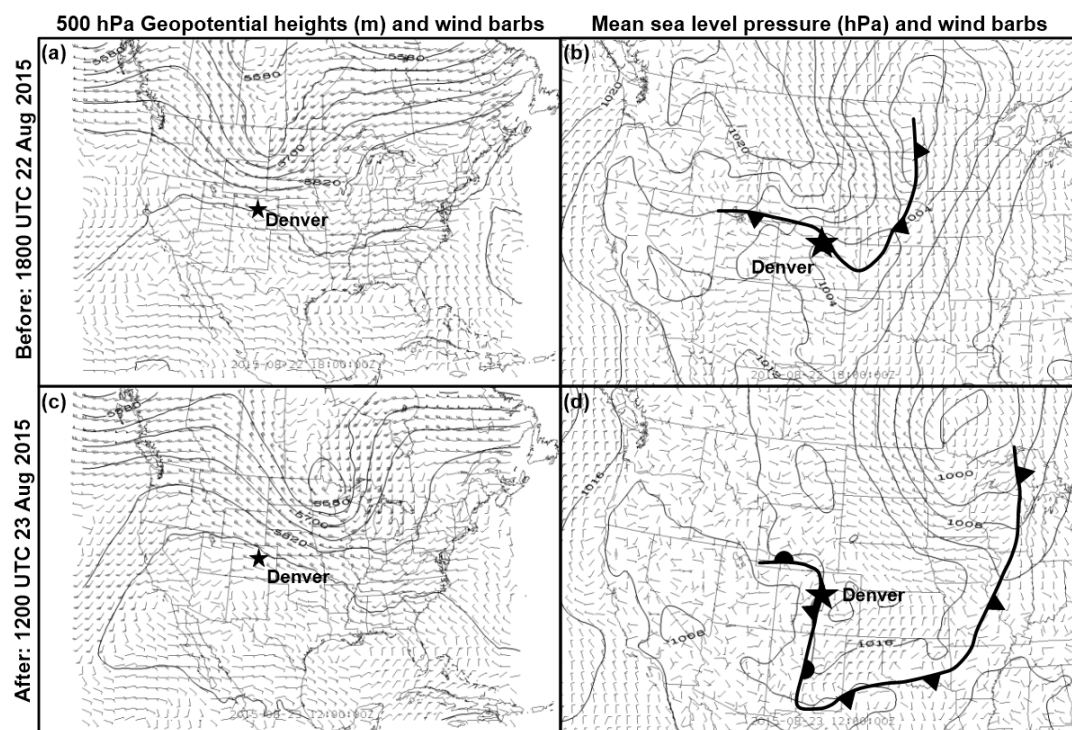
579

580 **Figure 8.** Air mass backward trajectories for all three cases where haze infiltrated the Front Range. Trajectories shown
581 were initiated every 6 hours during time periods (i.e., cases) surrounding each event (15–18 Aug 2015, 20–23 Aug 2015, and
582 26–29 Aug 2015 for Cases 1, 2, and 3, respectively), include those starting at 500, 1000, and 2000 m MSL, and extend back
583 10 days. Trajectories in red correspond to the haziest days (i.e., Events 1, 2, and 3 on 17, 23, and 29 Aug 2015, respectively)
584 during each case time period and the blue dashed trajectories show the remaining days that correspond to those in the
585 MODIS figures for each case.



586

587 **Figure 9.** Time-height section of hourly-averaged wind profiles for Event 1 from the 449-MHz wind profiler at BAO between
588 **0600 UTC 17 Aug and 0600 UTC 18 Aug 2015** (flags and barbs are as in Figure 7). The bold black line denotes the
589 **approximate frontal shear boundary**. The pair of red dashed lines shows the RAP analysis times before “B” and after “A”
590 **the cold-frontal passage at BAO during Event 1**. Time increases from right to left to portray the advection of upper-level
591 **synoptic features from west to east.**

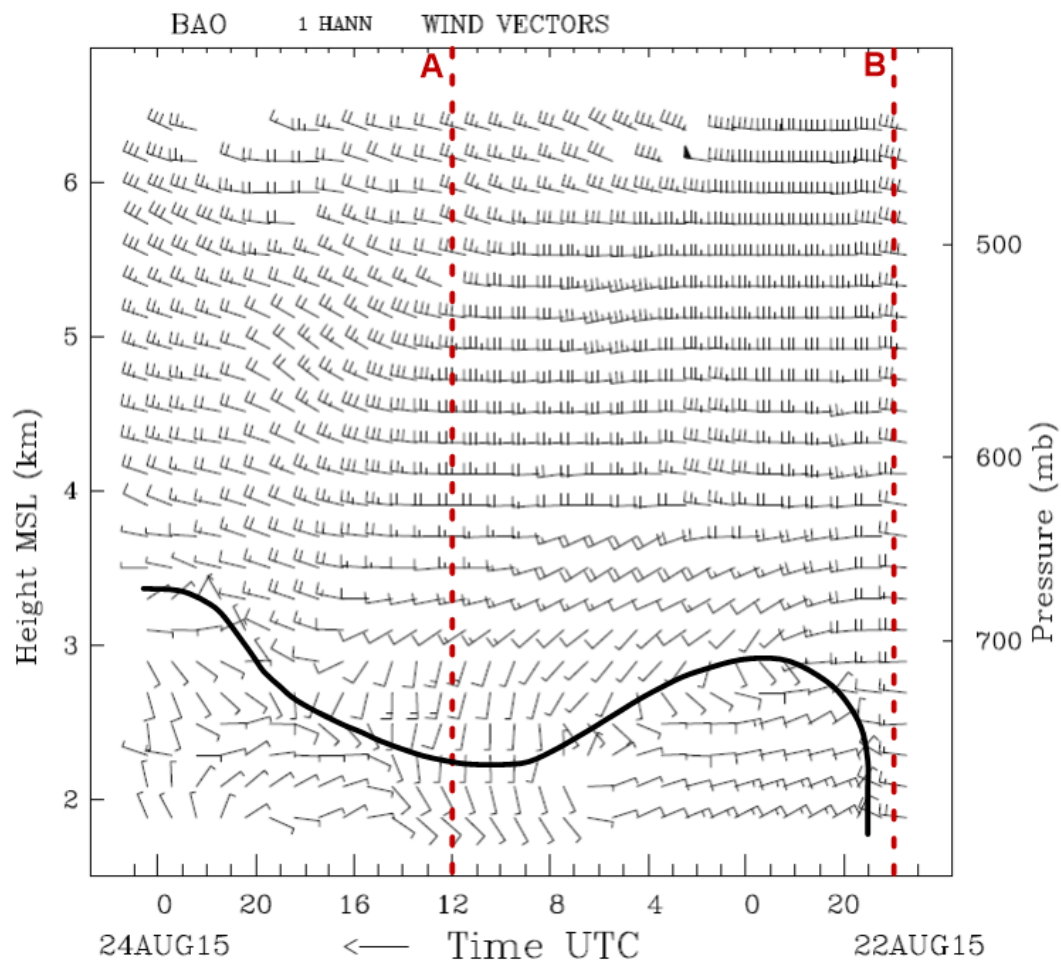


592

593

594

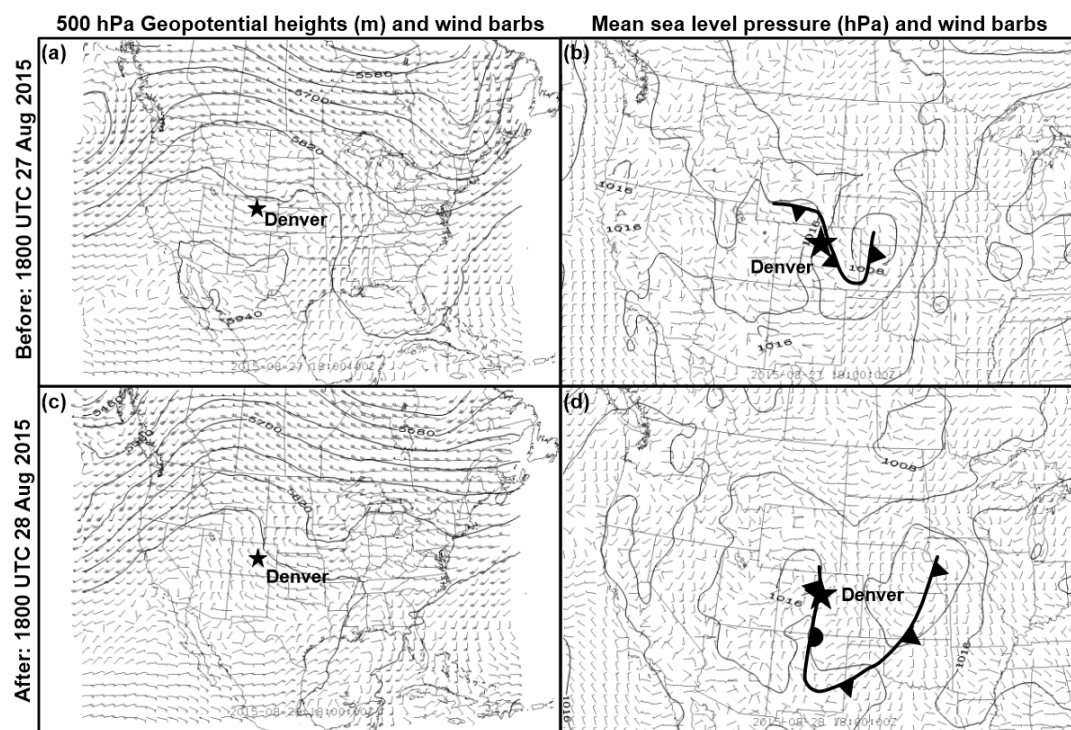
Figure 10. Same as Figure 7, but for before and after the cold-frontal passage of Event 2: 1800 UTC 22 Aug and 1200 UTC 23 Aug 2015, respectively.



595

596

Figure 11. As in Figure 9, but for the time period between 1700 UTC 22 Aug and 0100 UTC 24 Aug during Event 2.

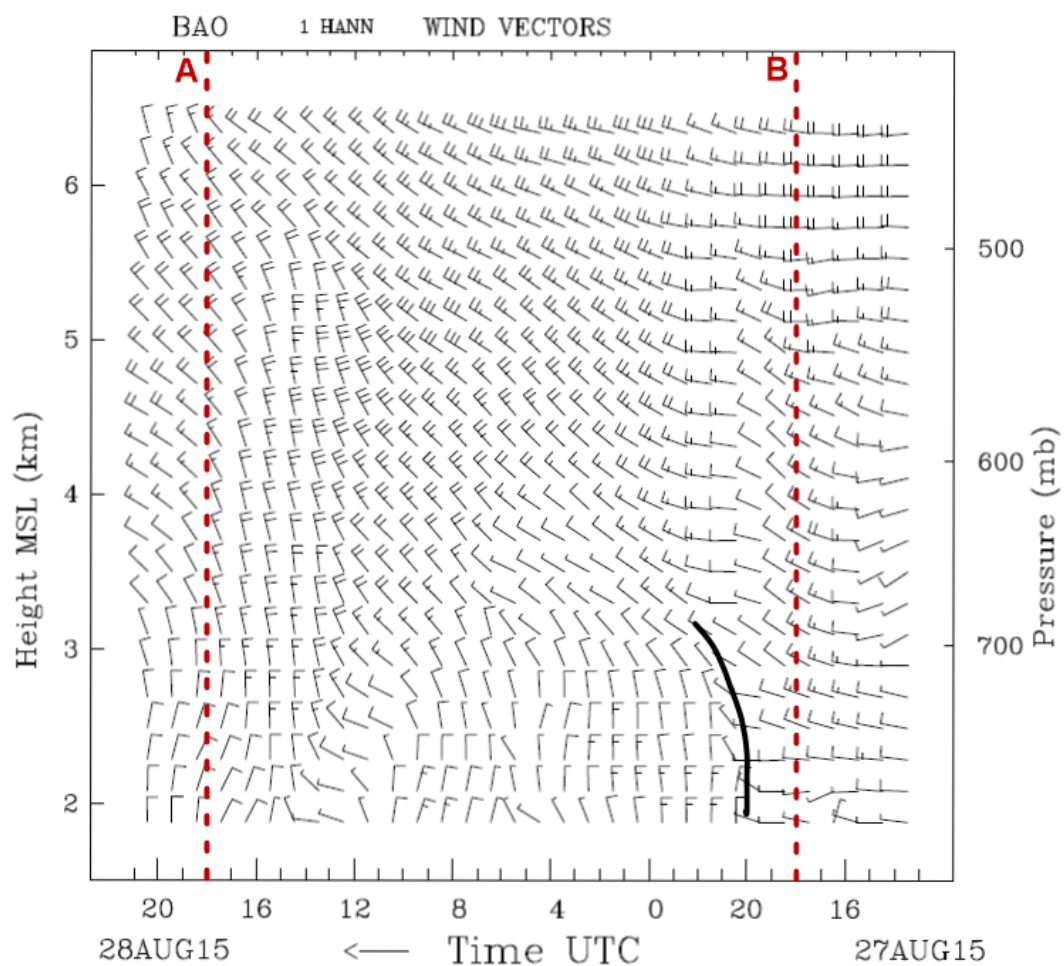


597

598

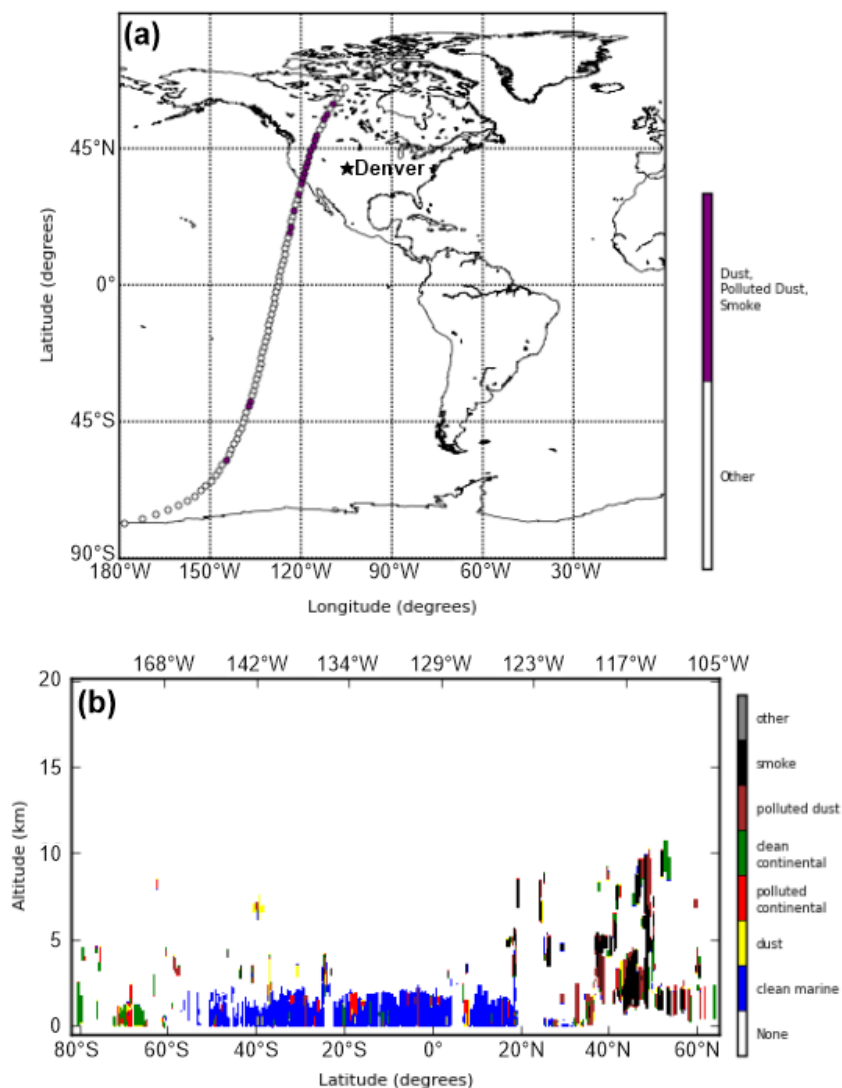
599

Figure 12. As in Figure 7, but for before and after the cold-frontal passage of Event 3: 1800 UTC 27 Aug and 1800 UTC 28 Aug 2015, respectively.

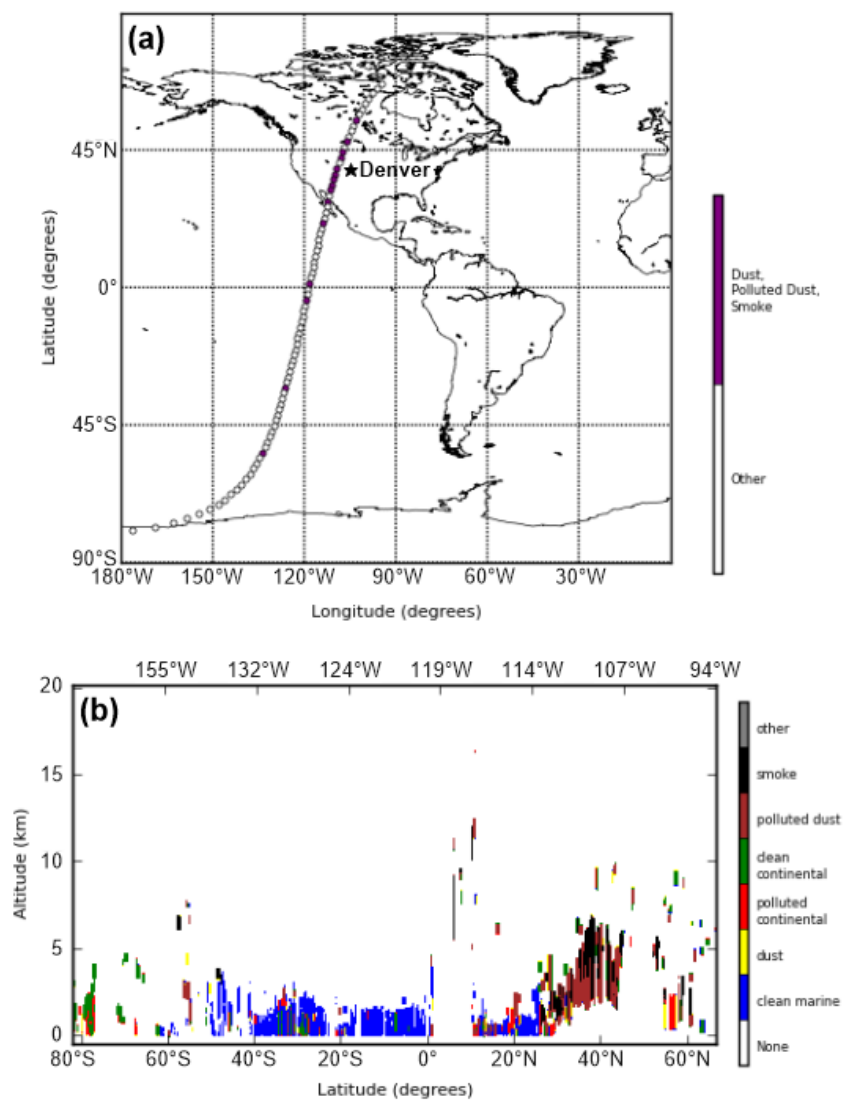


600

601 Figure 13. As in Figure 9, but for the time period between 1300 UTC 27 Aug and 2100 UTC 28 Aug during Event 3.

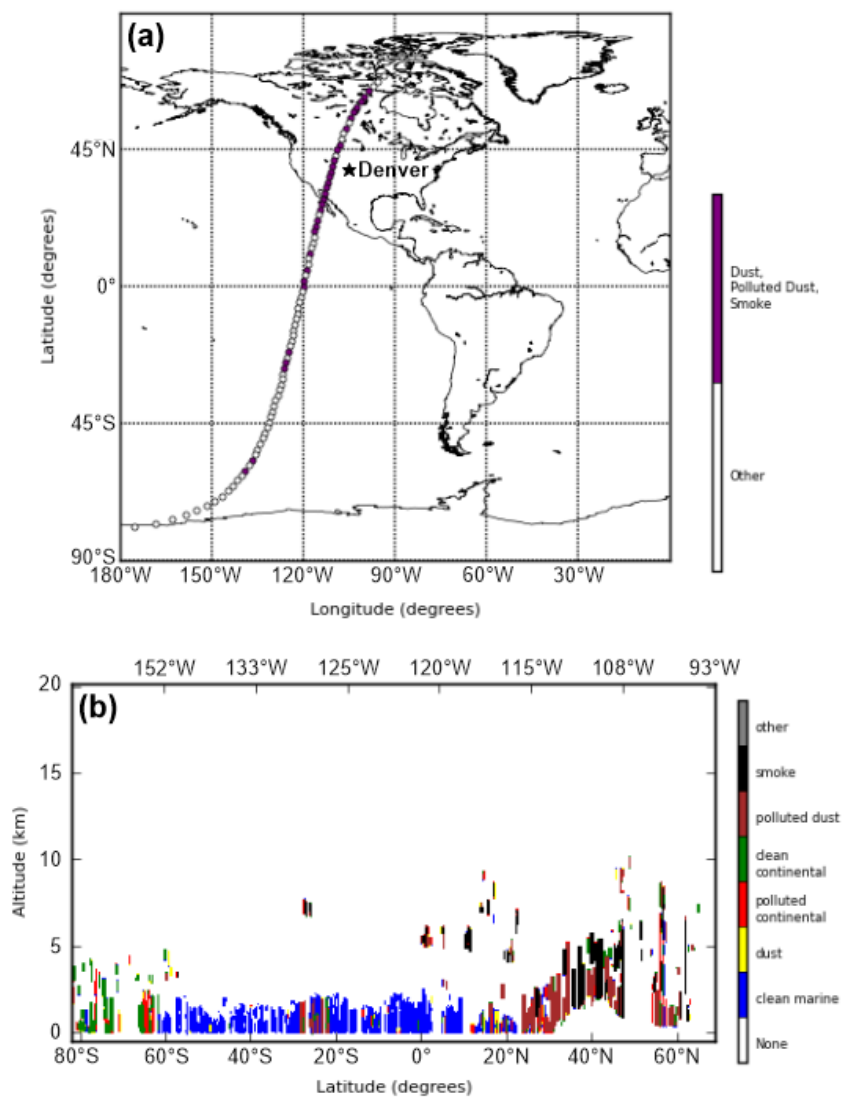


602
603 **Figure 14.** CALIPSO swath data from the night prior to Event 1. Swath data contained in CAL_LID_L2_VFM_ValState1-
604 V3-30 file from 16 Aug 2015 09:57:00 UTC. (a) Map showing CALIPSO coverage, with the purple markers representing
605 locations in the column measurement where dust, smoke, or polluted dust were observed. (b) Vertical profile (in km MSL)
606 for all aerosol subtypes of the swath corresponding to (a).



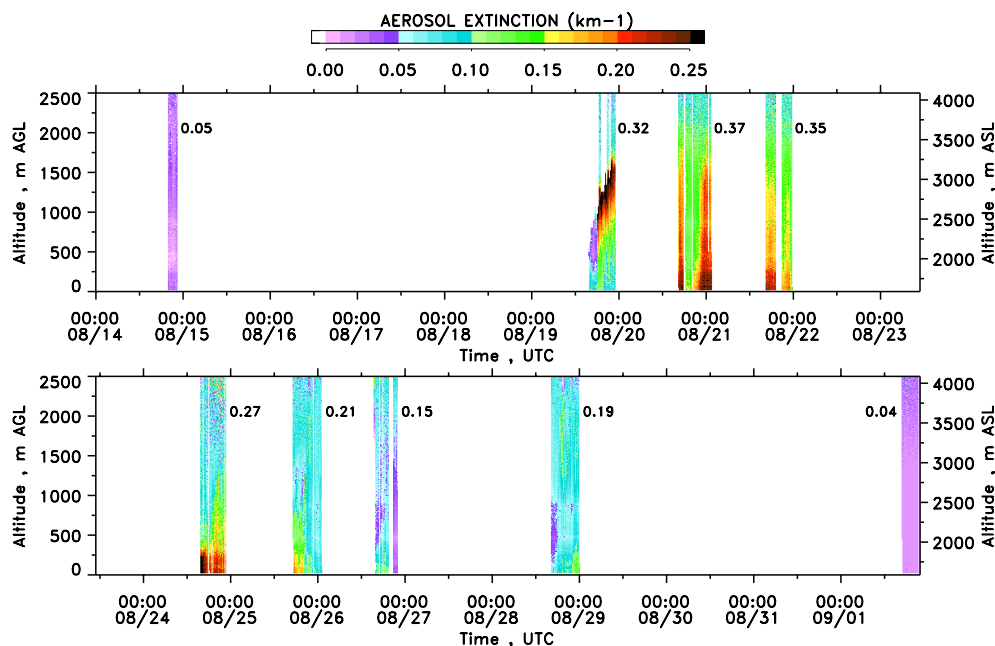
607

608 Figure 15. Same as Figure 14, but for the night prior to Event 2 and from 22 Aug 2015 09:19:24 UTC.



609

610 Figure 16. Same as Figure 14, but for the day of Event 3 and from 29 Aug 2015 09:24:15 UTC.

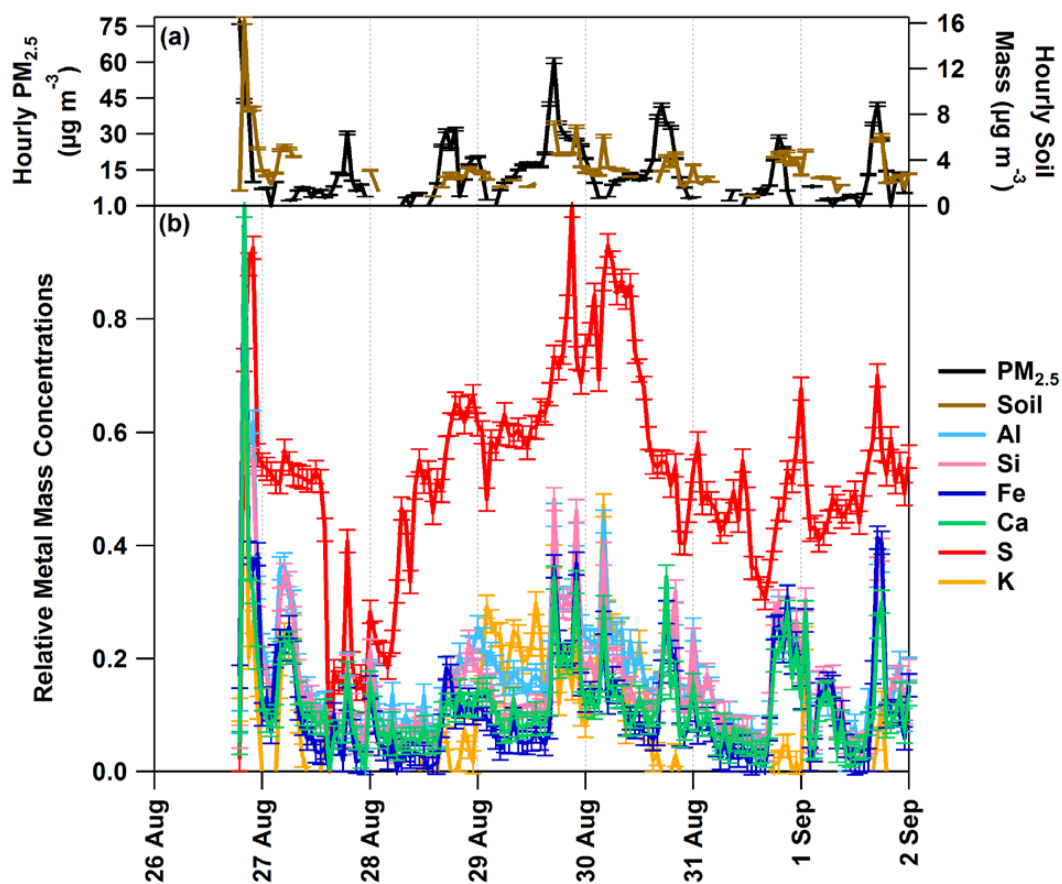


611

612 **Figure 17. Aerosol extinction profiles at 294 nm observed with the TOPAZ lidar on 9 days during the smoke pollution**

613 **episodes. The numbers next to each day's observations represent the daily mean AOD from the surface up to 2.5 km AGL**

614 **computed from the lidar measurements.**

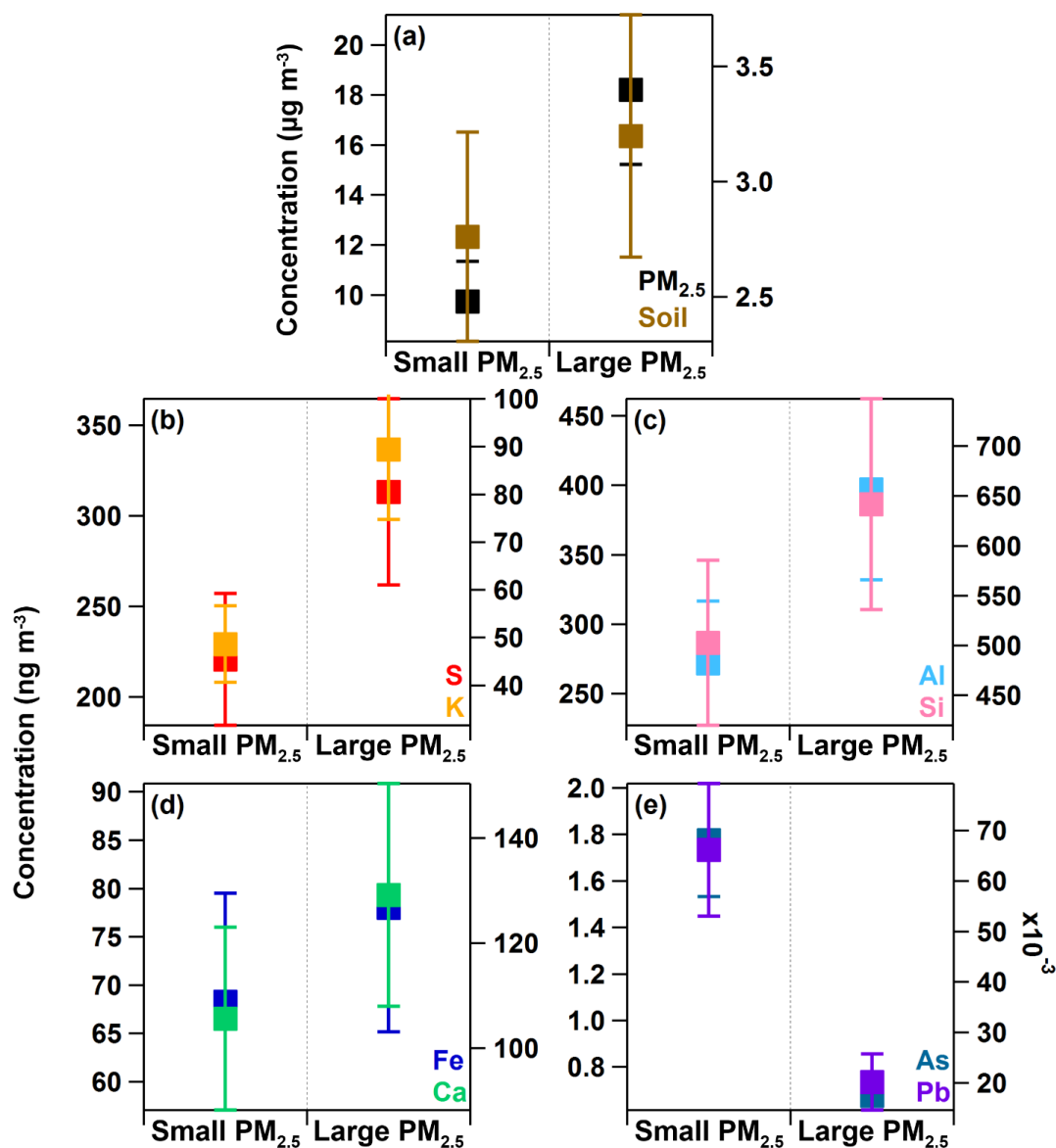


615

616 Figure 18. (a) Time series of hourly PM_{2.5} and soil mass concentrations as measured by PX-375 between 26 Aug and 2 Sep

617 2015 and (b) relative hourly mass concentrations of select individual metals over the LDLs, including an error of ±2%. PX-

618 375 data overlapped with Event 3.



619

620

621

622

Figure 19. Averages of PM_{2.5}, soil, and select metal mass concentrations during non-event days (i.e., cleaner conditions) compared to averages from haze event days (i.e., influence from fires haze) for 26 Aug–2 Sep 2015. Error bars represent the 90% confidence intervals.



Table 1. CDPHE sites used for particulate data within the Colorado Front Range. Each site has an ‘x’ for each measurement it maintained throughout the current work. Elevation is provided in meters above mean sea level (m MSL).

City/Site Name	Site ID	Latitude (degrees N)	Longitude (degrees W)	Elevation (m MSL)	PM _{2.5}	PM ₁₀
Boulder - CU/Athens	BOU	40.01	105.27	1,621	x	
Chatfield Park	CHAT	39.53	105.05	1,685	x	
Colorado College	CCOL	38.85	104.83	1,833	x	
Commerce City/Alsup Elementary	COMM	39.83	104.94	1,565	x	
Denver - Continuous Air Monitoring site	CAMP	39.68	104.99	1,610	x	x
Denver - National Jewish Health	NJH	39.74	104.94	1,615	x	
Fort Collins - CSU Facilities	FTCF	40.57	105.08	1,525	x	x
Greeley - Hospital	GREH	40.42	104.71	1,439	x	
I-25 - Denver	I-25	39.73	105.02	1,586	x	x
La Casa	CASA	39.78	105.01	1,601	x	x
Longmont - Municipal	LNGM	40.16	105.10	1,517	x	
Welby	WBY	39.84	104.95	1,554		x

PM_{2.5} = particulate matter with diameters $\leq 2.5 \mu\text{m}$

PM₁₀ = particulate matter with diameters $\leq 10 \mu\text{m}$

5

Table 2. Lower detection limits (LDLs, ng m⁻³) for metals measured by the PX-375 during 15 Aug–2 Sep 2015. Data less than the LDLs were excluded from analysis.

Species	LDL
Ti	2.29
V	0.23
Cr	0.61
Mn	0.93
Fe	1.51
Ni	0.33
Cu	0.78
Zn	1.21
As	0.02
Pb	0.80
Al	32.2
Si	5.17
S	1.11
K	4.37
Ca	1.18